Modeling Full-Envelope Aerodynamics of Small UAVs in Realtime

Michael S. Selig[*]

University of Illinois at Urbana-Champaign, Urbana, IL 61801, USA

This paper focuses on full six degree-of-freedom (6-DOF) aerodynamic modeling of small UAVs at high angles of attack and high sideslip in maneuvers performed using large control surfaces at large deflections for aircraft with high thrust-to-weight ratios. Configurations such as this include many of the currently available propeller-driven RC-model airplanes that have control surfaces as large as 50% chord, deflections as high as 50 deg, and thrust-to-weight ratios near 2:1. Airplanes with these capabilities are extremely maneuverable and aerobatic, and modeling their aerodynamic behavior requires new thinking because using traditional stability derivative methods is not practical with highly nonlinear aerodynamic behavior and coupling in the presence of high propwash effects. The method described in this paper outlines a component-based approach capable of modeling these extremely maneuverable small UAVs in a full 6-DOF realtime environment over the full envelope that is defined in this paper to be the full ± 180 deg range in angle of attack and sideslip. This method is the foundation of the aerodynamics model used in the RC flight simulator FS One. Piloted flight simulation results for four small RC/UAV configurations having wingspans in the range 826 mm (32.5 in) to 2540 mm (100 in) are presented to highlight results of the high-angle aerodynamics modeling approach. Maneuvers simulated include tailslides, knife edge flight, high-angle upright and inverted flight ("harriers"), rolling maneuvers at high angle ("rolling harriers") and an inverted spin of a biplane ("blender"). For each case, the flight trajectory is presented together with time histories of aircraft state data during the maneuvers, which are discussed.

Nomenclature

A	=	propeller disc area
a	=	airfoil lift curve slope (2π)
c	=	mean aerodynamic chord; camber
C_d	=	drag coefficient
C_l	=	lift coefficient
C_Q	=	propeller torque coefficient ($Q/\rho n^2 D^5$)
C_T	=	propeller thrust coefficient ($T/\rho n^2 D^4$)
$C_{m,c/4}$	=	moment coefficient about quarter chord
D	=	drag; propeller diameter
J	=	propeller advance ratio based on V_N
L	=	lift
M	=	pitching moment about y-axis (positive nose up)
n	=	propeller rotational speed (revs/sec)

[*]Associate Professor, Department of Aerospace Engineering, 104 S. Wright St. Senior Member AIAA.
http://www.ae.illinois.edu/m-selig

American Institute of Aeronautics and Astronautics

N_P	=	propeller yawing moment due to angle of attack
p, q, r	=	roll, pitch and yaw rate
P_N	=	propeller normal force due to angle of attack
Q	=	propeller axial torque
q	=	dynamic pressure ($\rho V^2/2$)
R	=	propeller radius
S	=	reference area
T	=	propeller axial thrust
u, v, w	=	components of the local relative flow velocity along x, y, z, respectively
V	=	flow velocity
x, y, z	=	body-axis coordinates, $+x$ out nose, $+y$ out right wing, $+z$ down
y_c	=	airfoil camber
TED	=	trailing edge down
TEL	=	trailing edge left
TEU	=	trailing edge up

Subscripts

N	=	normal component
R	=	relative component

Symbols

α	=	angle of attack ($\arctan(w/u)$)
β	=	sideslip angle ($\arcsin(v/V)$)
β'	=	angle of attack for vertical surface ($\arctan(v/u)$)
δ_a	=	aileron deflection [$(\delta_{a,r} - \delta_{a,l})/2$], right +TEU, left +TEU
δ_e	=	elevator deflection, +TED
δ_r	=	rudder deflection, +TEL
ϵ	=	wing induced angle of attack
η_s	=	dynamic pressure ratio for flow shadow (shielding) effect
ϕ, θ, ψ	=	bank angle, pitch angle, heading angle
ρ	=	air density
σ	=	propeller solidity (blade area/disc area)

Superscripts

$(\bar{})$	=	normalized quantity; average quantity

I. Introduction

There is growing interest in modeling and understanding full-envelope aircraft flight dynamics, that is, modeling the aircraft over the full ± 180 deg range in angle of attack and sideslip. Flight outside the normal envelope like this can be encountered in airplane stall/spin situations or more generally upset scenarios that can be caused by a host of factors – pilot, aircraft, weather, etc. Moreover, aerobatic airplanes routinely enter and exit controlled flight "outside-the-envelope" with precision and grace. Interest in full-envelope aircraft flight dynamics has also been fueled in recent years by the rapid growth in UAVs (both civilian and military) together with synergistic parallel advances in high-performance RC model aircraft.

Within the broad spectrum of UAV/RC configurations has emerged a general category that is capable of extremely agile maneuvers such as V/STOL-like flight, hovering, perching, stop-and-stare, defensive and evasive postures and rapid roll, pitch, yaw rates and accelerations.[1–7] The high agility derives from having control surfaces as large as 50% chord with deflections as high as ± 50 deg and propeller thrust-to-weight ratios of near 2:1. A tractor-propeller-driven fixed-wing RC variant that falls in this category is shown in Figure 1 with the large control surfaces at neutral and then deflected to illustrate their full extent.

These ultra-agile configurations clearly present new challenges to flight dynamics simulation and modeling because of the combined considerations of high-angle full-envelope flight, large highly-deflected control surfaces, strong propeller wash effects, high thrust and concomitant unsteady flow. In the general case,

American Institute of Aeronautics and Astronautics

Figure 1. Extra 260 ultra-agile aerobatic foam-construction electric propeller-driven RC aircraft with large control surfaces at neutral and maximum deflections [wingspan of 826 mm (32.5 in)].

modeling ultra-agile aircraft over the full envelope is not likely to be successful using a stability-derivative approach because of the strong nonlinearities and coupling effects. Physical wind-tunnel measurements also fall short of capturing the aerodynamics of the full static and dynamic envelope due to a number of factors, e.g. the sheer time and expense of a full test campaign as well as the most basic issue of wind tunnel wall effects such as propeller wash recirculation within the test section.[8] One might envision using a brute force CFD analyses to generate lookup table data for a full vehicle, but the computational resources needed to cover a typical flight envelope in a reasonable period of time exceed current-day capabilities.[9–11] Although modeling agile static and dynamic flight presents a plethora of challenges for CFD techniques, some new approaches might make it more feasible to consider in the future.[12] Aircraft system identification methods,[13,14] as with all of the aforementioned techniques, could be used to provide insight in special cases, but general application of the system ID methods to full-envelope aerodynamics modeling would be daunting, and it has not been proposed.

With the primary objective of this research being full-envelope 6-DOF simulation, a feasible approach after considering some of the alternatives is to use a component buildup methodology that relies as much as possible on first-principles aerodynamics modeling supported by lookup tables for any data that can be obtained a priori, e.g. aerodynamic coefficient data covering the full ±180-deg range. As with any component buildup approach, evaluation of the component forces and moments can rely on data from myriad sources, e.g., wind tunnel measurements, analytical predictions, CFD results, and empirical/semi-empirical methods. The superposition of all elements of the model, taking into account any appropriate interaction effects, then yields the summation of all forces and moments acting on the total vehicle airframe. This general approach has been applied to a wide range of problems in modeling and simulation, for example, propeller-dominated UAV flight dynamics,[5,6,15] ducted fan configurations,[16] autonomous underwater vehicles,[17] wing-only tumbling analysis,[18] high angle of attack longitudinal aircraft trim analysis,[19] and post-stall flight dynamics and upset modeling[20–24] to name a few.

As described in this paper, a component buildup method was developed for ultra-agile UAV/RC aircraft. In particular, the full-envelope aerodynamics modeling framework described here is that which is implemented in realtime in the FS One™ RC flight simulator.[25] This paper focuses on the methods used in modeling the wing, fuselage, and tail surfaces of a conventional, yet highly maneuverable, aerobatic configuration. Propeller effects are included in the method and discussed, but a more in-depth description of the propeller aerodynamics modeling is included in a companion paper.[26] Example maneuvers predicted by the method are illustrated and discussed. It is worth adding that while components can be added to the method they can also be removed and as such easily and realistically simulate damaged aircraft or faulty system components.[27]

II.   Model Requirements

In this research, the requirements from the outset were to create a realtime simulation environment capable of modeling the flight dynamics of small, agile UAV/RC configurations. As stated, these vehicles

American Institute of Aeronautics and Astronautics

have high thrust-to-weight ratios near 2:1 and use large control surfaces at high deflections immersed in strong propeller wash. Consequently, the trimmable flight envelope is large, and the range of dynamic maneuvers is spectacular.

The trimmable flight envelope to be captured in simulation includes all of the nominal trimmed states, e.g., straight flight and turning flight. While normal cruise flight is the nominal condition, these highly maneuverable UAV/RC aircraft can fly outside the envelope in trim at high angles of attack near 45 deg with large nose-up elevator input – the so-called "harrier" maneuver in RC parlance. This flight condition relies on lift from the wing and also the vertical component of thrust to sustain level trimmed flight. Taken further with more nose-up elevator and additional thrust the flight can be arrested to a 90-deg angle of attack stationary hovering attitude that uses only thrust to support the aircraft weight. This hover condition can also be entered from steady knife-edge flight that is extended with large rudder input to an extreme 90-deg yaw that again ends in a stationary hovering attitude. All of these conditions were required to be captured in the simulation.

Apart from trimmed flight, other dynamic maneuvers to be captured by the simulation are much more complex. These include the classic stall from upright longitudinal flight and also wing tip stall that can precipitate into a fully-developed spin. The spin can be characterized by a number of descriptors, e.g., it can be an upright spin or inverted spin with either a nose-down attitude or flat spin with power added or not, all resulting in extremely complex aerodynamic states to model. "Blender" is the particular name given to inverted power-on flat spins that are dramatic, and this same maneuver can be entered and momentarily sustained from a level high-speed flight condition. Snaps, tailslides, hammerheads and knife edge stall are also dynamic maneuvers that are aerobatic in nature and lead to high-angle flight conditions. Modern RC models with high thrust capabilities can also perform what are called "rolling harriers," which is a high angle of attack slow roll condition that requires modulating elevator and rudder input (out-of-phase) to keep a nose-high attitude while simultaneously rolling with near constant aileron input. These rolling harriers can be flown in straight flight, turning flight, loops or horizontal (or vertical) figure eights, etc. Other rapid maneuvers to extreme angle are "walls" (rapid pitch up from level flight to an arrested hovering position), "parachutes" (rapid pitch to level from a vertical downline), and "elevators" which is a deep-stall descent attitude. Apart from upset conditions that are accidentally encountered, these aerobatic dynamic maneuvers and others that are well known (e.g., torque rolls, "waterfalls" and knife-edge loops) clearly depend on varying degrees of pilot skill to perform. Simulating these maneuvers poses unique and formidable challenges in aerodynamics modeling.

Other simulation requirements factored into the original design and having impact on the aerodynamics modeling included the following. First, the environment was required to be capable of simulating many different aircraft and thus not be tailored to capturing only the flight dynamics of certain special maneuvers unique to one or a few aircraft. Second, simulating the effects of damage or missing parts (e.g., a failed aileron or a missing wing) was key initially because of the commercial market appeal, but including these features has longer reach and applies to failures of full-scale aircraft as well. Third, the simulation environment was required to allow for automatic scaling of any native aircraft to any other size, e.g., nano-scale, micro-scale, 50%-scale and full-scale. Fourth, because typical small aircraft are subject to relatively high atmospheric turbulence, a robust wind and turbulence model was required in the simulation.

Finally, the simulation framework (including graphics, physics, pilot inputs, recording features, and more) was required to run in realtime on a standard gaming-level desktop PC. Clearly, this computational environment set additional requirements on the aerodynamics modeling methodology to make it robust and also capable of simulating nominal, agile and aerobatic flight over a range of situations. The remainder of this paper henceforth will focus on the aerodynamics modeling and simulation that achieves all of the broad requirements that have been outlined in this section.

III.   Technical Development Process

The development began with a relatively simple and general approach – that of using stability derivatives. However, during the core development period (3 yrs), each element of the stability derivative approach was replaced by methods that could capture the full envelope with enough generality to simulate flight in any attitude.

Out of this fundamental bottom-up approach arose the capability to simulate highly nonlinear complex

American Institute of Aeronautics and Astronautics

maneuvers that are observed in actual flight across a spectrum of aircraft. In fact, the framework was applied equally across an array of more than 30 aircraft covering myriad configurations that ranged from simple rudder-elevator glider trainers to ones having propulsion (jet and propeller) with large flaps, ailerons, elevator, and airbrakes.[25] The technical development also directly benefited from and depended on the author's 40-yr experience with flying and observing model aircraft as well as physical measurements, flight video and feedback from professional RC pilots and aircraft designers.

IV.   Component Aerodynamics Models

In the model, the aircraft is divided into basic components such as the wing, horizontal tail, vertical tail, propeller, etc., and for each a separate model is developed to determine the contribution that each component makes to the total forces and moments on the aircraft at each point in time. For each component, the local relative flow is determined taking into account aircraft speed and rotations (assuming rigid body kinematics) together with wind, turbulence and any aerodynamic interference effects such as propeller wash, wing induced flow, shielding effects (e.g., tail blanketing in spin), ground effect and more. For most of the models, the component state (relative flow, surface deflections, and other data as it might apply) is then used to determine any related aerodynamic coefficient data. The final component dynamic pressure, aerodynamic coefficient data and respective reference area are then used to determine the forces and moments. This basic approach applies to the simplest component models, while in most cases additional steps are taken or an entirely different approach is used involving analytical and/or empirical/semi-empirical methods built upon some physical basis.

A.   Wing Aerodynamics

The wing aerodynamics produce the most dominant forces and moments, and thus careful modeling is key to simulating full vehicle performance. Challenges in predicting this performance include mainly high angle (± 180 deg) performance and large control surfaces at high deflections. Other important elements include wing-in-propeller slipstream effects, induced flow produced by the wing, shielding of one wing on another (biplane wings), apparent mass and flow curvature effects. In most cases the reduced frequency in pitch is small enough that dynamic stall effects are small, and thus this effect is not currently included in the model.

In order to run in realtime, there must be a balance between using on-the-fly fundamental physics methods and pre-computed data that can be accessed quickly through lookup tables. For the wing, this precomputed data includes the full aerodynamic coefficients (C_l, C_d, $C_{m,c/4}$) and induced angle of attack as a function of any control surface deflections. These data are local values at stations along the wing, that is, the wing is discretized and in the simulation a strip theory approach is applied as will be described.

As a method, strip theory is used for aircraft aeroelastic simulations[28] and routinely for blade element theory in the rotorcraft field.[29] Strip theory approaches have also been applied to wings in a trailing vortex flow and aircraft spin prediction (see Refs. 30–33 and others cited therein). It seems that only recently has the general strip theory approach been applied in realtime simulation for fixed-wing force and moment calculations.[6,23,24]†

Various approaches to implementing a strip theory approach have been applied for fixed and rotary wing aircraft. In this work, the approach is to use a nonlinear lifting line code to determine the local induced angle of attack at each section along the wing over a range of angles of attack and control surface deflections. Thus, lookup tables are created for the local 2D induced angle ϵ as a function of the local 2D angle of attack α and local control surface deflection. In the method, the local 3D flow for an element of the wing is composed of the sum of all velocity components due to aircraft motion, propeller wash, and wind along with corrections for any shielding that might be modeled on the element. From this direct flow calculation, the local 2D angle of attack is obtained and used to find induced angle through lookup tables. A ground effect correction is also applied when in ground proximity. Taking all these contributions into account, the angle of attack of the relative flow becomes

$$\alpha = \alpha_{\text{direct flow}} + \epsilon + \Delta\alpha_{\text{ground effect}} \tag{1}$$

---

†In this work in the development of FS One, the strip theory approach was used from the outset beginning in 2003. It should be mentioned that a strip theory approach is used in the X-Plane™ commercial flight simulator as briefly mentioned online by the company, see `http://www.x-plane.com`.
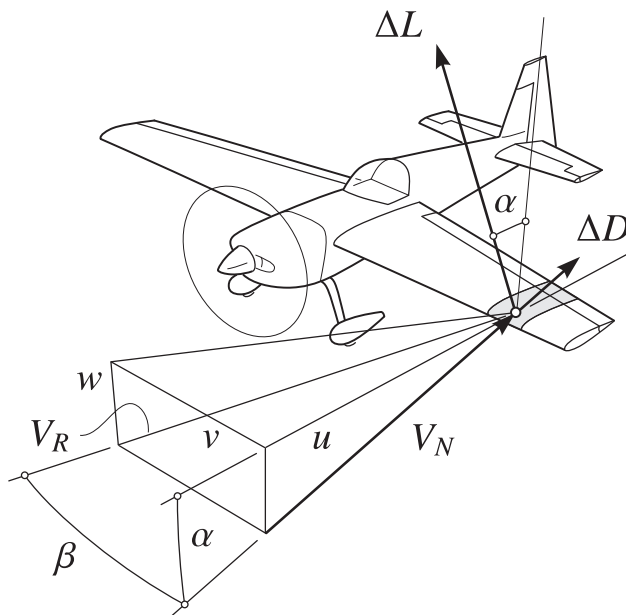
Figure 2. Convention showing local flow for a strip of the wing and resulting in-plane lift and drag.

Figure 2 shows this angle of attack for an element of the wing along with the local normal flow component V_N corresponding to the local relative flow V_R. Using the angle of attack, the corresponding section lift, drag and moment coefficients are found through lookup tables, and if the section operates in the post-stall regime some corrections are applied. The resulting lift, drag, and moment at the quarter chord location of the element are given by

$$\Delta L = q_N \Delta S C_l \tag{2}$$
$$\Delta D = q_N \Delta S C_d \tag{3}$$
$$\Delta M = q_N \Delta S C_{m,c/4} \tag{4}$$

where

$$q_N = q_R \cos^2 \beta \tag{5}$$

The resulting location of the element is then used to transfer these data to the aircraft center of gravity.

The approach relies on a great number of lookup tables that are interpolated in realtime. For a typical wing, 20 elements may be used along the wing with some elements naturally aligned on the edges of control surfaces, at dihedral breaks, or positioned inside the propeller wash. Each element includes its associated tables for lift, drag and moment coefficients as well as local induced angle of attack. Other tables are included to account for any propeller wash and shielding that may exist depending on the position of the element along the wing. Thus, at a minimum, a typical wing during realtime execution will use 80 tables of data and more if additional effects are included. For a biplane, the number of tables for the wing system doubles.

The ShowTime 50 shown in Fig. 3 is representative of some popular RC aerobatic configurations with large control surfaces that can be deflected to high angles. The aircraft is produced and distributed by Hangar 9™, and a scaled-down variant has been examined recently in experiments designed to study wing rock.[34] As seen in Fig. 3, the 1.45-m (57-in) wingspan aircraft has wing side-force generators (which are optional) for greater performance in knife-edge flight. The particular control surface sizes for the ShowTime 50 are shown in Fig. 4 for the inboard aileron, elevator and rudder for deflections of 15, 30 and 50 deg.

Aerodynamic performance characteristics for these high deflections for the full range cannot yet be reliably predicted using CFD; however, there are a number of numerical and experimental sources of data that can be used as guides in generating the necessary data over the full angle of attack range of ±180 deg. For the wing airfoil, the data fusion process combines any available experimental data with predictions from XFOIL[35] for low angles of attack and small flap deflections, and for high flap deflections and high angle of

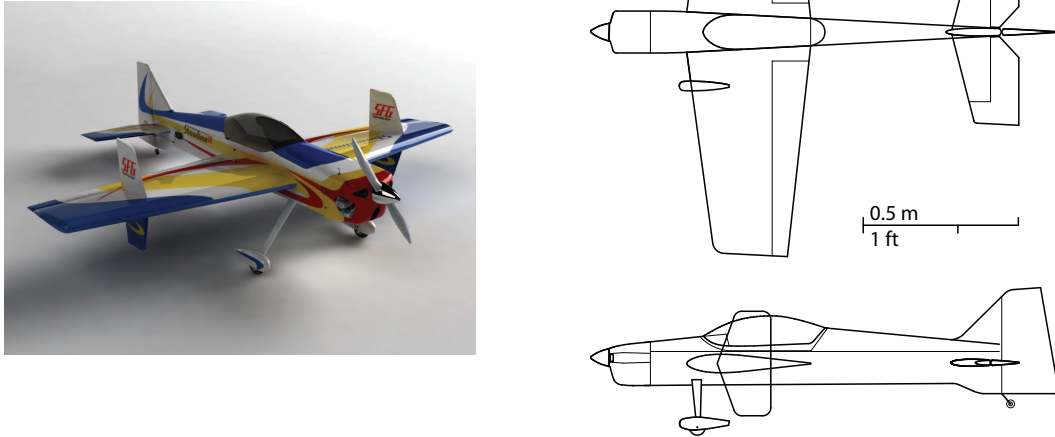American Institute of Aeronautics and Astronautics

Figure 3. ShowTime 50 aerobatic RC aircraft configured with elevator, rudder, ailerons and wing dual side-force generators (graphics rendering by Rick Deltenre).

attack (including reverse flow beyond ±90 deg) semi-empirical techniques are employed to yield results like those shown in Fig. 5. These particular results are for the ShowTime 50 inboard wing airfoil, but many of the trends in the post-stall region are similar across a range of airfoils with differences depending largely on airfoil thickness, camber, control surface size and leading-edge radius. Figures 6 and 7 present the lift and drag coefficient data as the lift-to-drag (C_l/C_d) ratio and in airfoil polar (C_l-vs-C_d) format, respectively. These are convenient ways of viewing and interpreting the data, and it makes for easy comparison across a range of literature (airfoil data for aircraft, sailing, motorsports, and wind energy). Because the wing airfoil shown in Fig. 4 is symmetrical, the data shown in Figs. 5–7 reflects this fact.

From the known wing geometry and airfoil data as shown, a nonlinear lifting-line code is used to determine the local induced angle of attack for a given wing angle of attack and control surface deflection. The procedure starts with an estimated circulation distribution $\hat{\Gamma}_i$ along the wing. From this estimate, the downwash distribution $\hat{w}_i$ is obtained using Biot-Savart law, and this is used to determine the local lift coefficient $\hat{C}_l$ using lookup tables based on data like that shown in Fig. 5. With this lift coefficient and the local geometric properties, a new estimate for the circulation $\hat{\Gamma}_{\text{new}}$ is determined. If this new estimate matches the initial values within a small, specified tolerance, the solution has converged; otherwise, the iteration continues with under-relaxation being used to obtain a new estimate for the circulation determined by

$$\hat{\Gamma}_{i+1} = \omega\hat{\Gamma}_{\text{new}} + (1 - \omega)\hat{\Gamma}_i \tag{6}$$

This process is repeated for a 2D sweep over the control surface deflections and angle of attack (nominally -20 deg $< \alpha < 20$ deg), and the data is saved as a lookup table. During realtime simulation, the induced angle of attack is tapered to zero at the limits at an absolute angle of attack of 90 deg. Thus, beyond ±90 deg, the induced angle of attack is assumed to be zero which is reasonable considering that at 90 deg the wing lift is nearly zero, and beyond this point the aircraft remains in this state (in reverse flow) only momentarily while most likely undergoing large angle of attack excursions, e.g., in a tailslide maneuver.
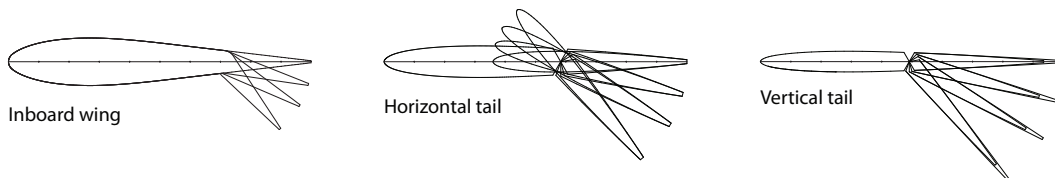

Figure 4. Airfoil sections used on the ShowTime 50 with control surface deflections of 15, 30 and 50 deg.
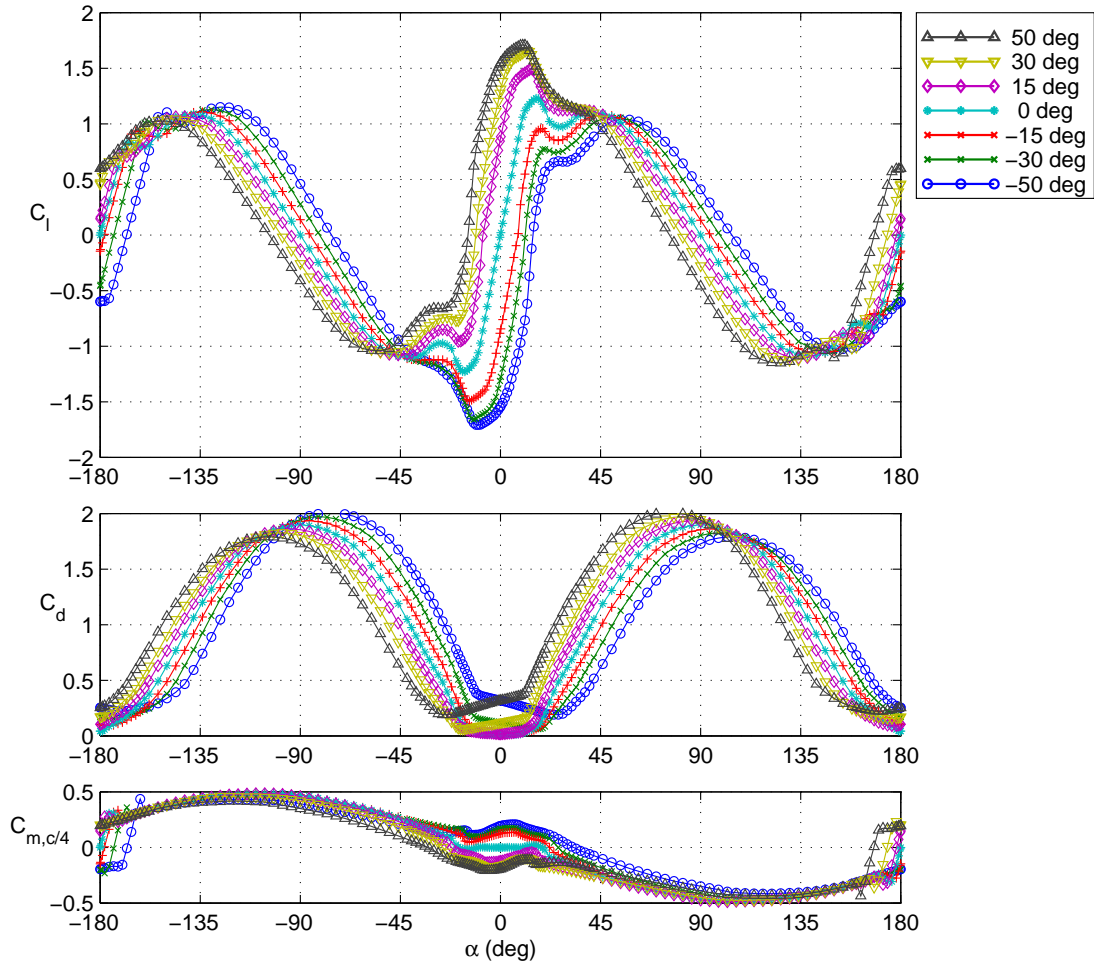
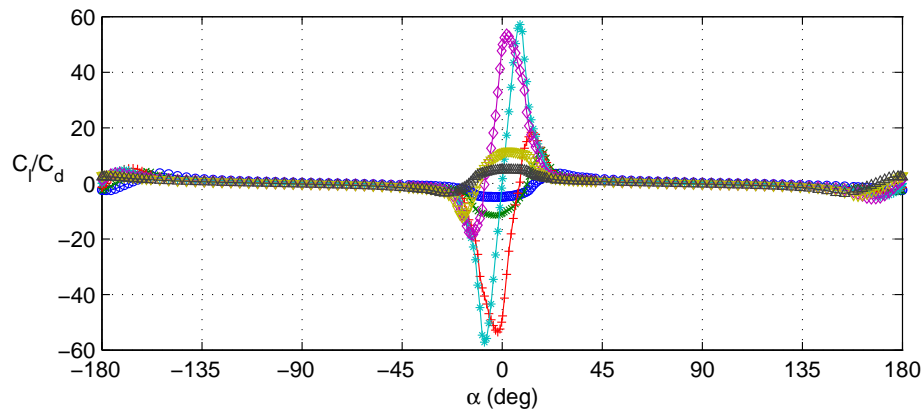**Figure 5. Airfoil performance over the full ±180-deg angle of attack range for aileron deflections of 0, ±15, ±30, and ±50 deg.**

Figure 6. Airfoil lift-to-drag characteristics over the full ±180-deg angle of attack range for aileron deflections of 0, ±15, ±30, and ±50 deg (see Fig. 5 for legend).

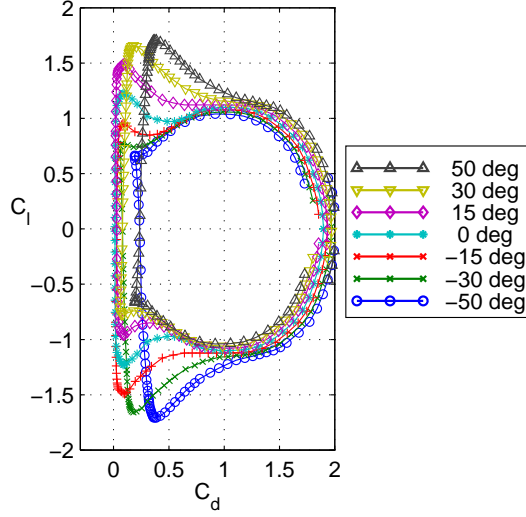As seen in Fig. 5, around an angle of attack near 90 deg the drag coefficient C_d is ≈ 2 and consistent

American Institute of Aeronautics and Astronautics

Figure 7. Airfoil polar over the ±90-deg angle of attack range for aileron deflections of 0, ±15, ±30, and ±50 deg.

with flat plate theory with corrections that were developed for control surface deflections. For a wing with a moderate aspect ratio, however, the drag coefficient C_D at 90 deg is lower than the 2D case,[36] thus an additional correction must be used to take this into account. For a flat plate wing at an angle of attack of 90 deg, the pressure on the downstream leeward side is nearly constant because the separated flow cannot support a pressure gradient, and this result can be seen in pressure distributions of wind turbine blades at 90 deg to the flow.[37,38] Consequently, the drag coefficient in the 90-deg case will be nearly constant along the entire wing, and CFD predictions for flat plate wings are consistent with this fact.[39] Hence, when the flow is completely separated (beginning after stall), approximately constant pressure on the downstream side of the wing is maintained, and as complex as the flow may seem, a 2D assumption and hence the strip theory approach can still be used as a model of the flow. This thinking was applied in creating the post-stall 3D corrections to the 2D airfoil data.

Figure 8 shows the non-flapped airfoil data for the symmetrical ShowTime 50 airfoil shown in Fig. 5. The data is corrected for 3D post-stall effects as follows. For the 90-deg case alone, various empirical curve fits have been given for the wing drag coefficient $C_{D_{90}}$ as a function of the wing airfoil drag coefficient $C_{d_{90}}$ and wing aspect ratio AR.[40] In this development, it is necessary to form a correction that applies not just at 90 deg but over the entire post-stall range of angles of attack. The full-envelope 2D-to-3D correction used here begins with a modification of the 90-deg case given by Lindenburg,[41] namely

$$C_{d_{90}} = 2.2\{1 - 0.41[1 - \exp(-17/AR)]\} \tag{7}$$

where here the wing aspect ratio AR is used instead of an effective aspect ratio AR_{eff} used by Lindenburg. This value $C_{d_{90}}$ is simply normalized to provide scaling factor used in the next step, that is

$$k_{C_d} = C_{d_{90}}/2.2 \tag{8}$$

The final drag used for each element of the wing is then given by

$$C_{d,\text{corrected}} = C_d[1 - w(1 - k_{C_d})] \tag{9}$$

where w is a cosine weighting function expressed as

$$w = \cos\left[\pi\left(\frac{\alpha - \alpha_{P,1}}{\alpha_{N,2} - \alpha_{P,1}}\right) - \frac{\pi}{2}\right] \tag{10}$$

where $\alpha_{P,1}$ and $\alpha_{N,2}$ define the range over which the correction applies, tapering to zero at the ends. Furthermore, to maintain the necessary relationship that $C_L/C_D \approx 1/\tan\alpha$ (see Ref. 42), the same correction
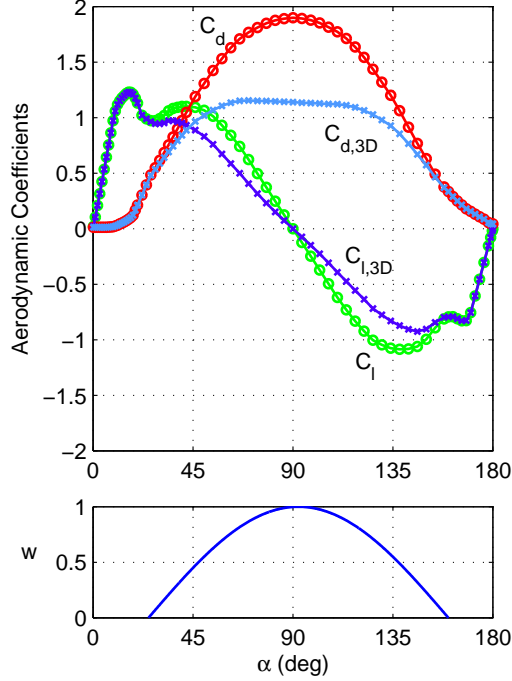
American Institute of Aeronautics and Astronautics

Figure 8. Application of post stall correction method for $AR = 4.5$ **showing the uncorrected airfoil data, corrected airfoil data ("3D"), and weighting function** w **used in the correction for the angle of attack range of 0 to 180 deg.**

is applied to the local lift coefficient, viz

$$C_{l,\text{corrected}} = C_l[1 - w(1 - k_{C_d})] \tag{11}$$

Moreover, since the moment in the post-stall region is driven largely by drag acting on the 50% chord location (the center of pressure), the correction also applies to the moment coefficient, viz

$$C_{m,c/4,\text{corrected}} = C_{m,c/4}[1 - w(1 - k_{C_d})] \tag{12}$$

Figure 8 shows the application of this approach over the range of 0 to 180 deg for the inboard wing airfoil lift and drag coefficient data for the zero aileron deflection case that was previously presented in Fig. 5. The original airfoil data is shown together with the corrected data and the cosine weighting function applied over the range -25 deg to 160 deg, which approximately defines the post-stall region for this airfoil. More sophisticated approaches[43] could be used for blending in the corrections (via the weighting function, Eq. 10), but the current approach closely models experimental data and has the benefit of being computationally efficient.

Other important effects modeled include quasi-steady aerodynamics produced by pitch-rate induced airfoil camber.[44,45] A positive pitch rate increases the lift coefficient and moment. Only the pitch-rate effect on lift is discussed here. The effective camber produced by the pitch rate can be approximated from its geometry by

$$(y_c/c)_{\text{eff}} = 0.54 \, \frac{c}{2} \, \sin(\Delta\alpha_c/2) \tag{13}$$

where

$$\Delta\alpha_c = \frac{\dot{\alpha}c}{u_R} \tag{14}$$

The pitch-rate increment in section lift coefficient is then obtained from

$$\Delta C_{l,\text{due to pitch rate}} = (y_c/c)_{\text{eff}} \, \frac{\partial C_l}{\partial(y_c/c)} \tag{15}$$
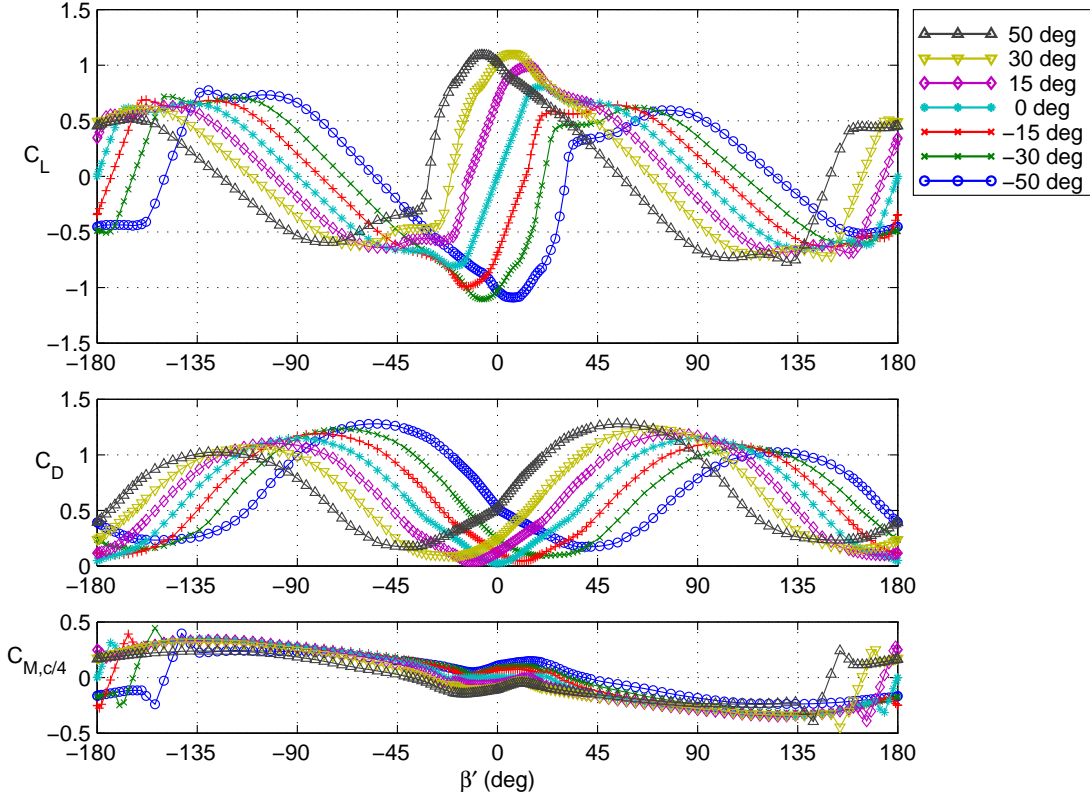
American Institute of Aeronautics and Astronautics

Figure 9. Vertical tail performance over the full ±180-deg side angle of attack range for rudder deflections of 0, ±15, ±30, and ±50 deg.

where it is taken that $\partial C_l / \partial (y_c/c) = 11.25$. The final section lift increment is close to that obtained from quasi-steady thin airfoil theory when the pitch occurs about the 50% station, in which case there is no additional pure angle of attack contribution. This latter additional contribution from thin airfoil theory and plunge effect are not included here because these effects are already accounted for by using the relative velocity approach for all components. Taking into account 3D effects, the resulting increment in wing lift coefficient becomes

$$\Delta C_{L,\text{due to pitch rate}} = \Delta C_{l,\text{due to pitch rate}} \left(\frac{AR}{AR+2} \right) \tag{16}$$

Finally, in realtime simulation, to avoid any physically unrealizable ΔC_L values determined by this method (e.g., caused by a spike in $\dot{\alpha}$ produced by a rapid nose-up bounce upon landing), the computed increments are limited to narrow range, e.g., $\Delta C_L \approx \pm 0.1$.

B. Tail Surface Aerodynamics

Unlike the wing, the tail surfaces are modeled as full surfaces without the use of strip theory. As with the wing, the aerodynamics of the tail surfaces are modeled over the full ±180-deg range in angle of attack and sideslip. As shown in Fig. 4, the flap sizes and maximum deflections can be extreme, and this requires relying partly on semi-empirical methods to capture the full-envelope performance. Wash models are also taken into account. First, the propeller wash on the tail surfaces is especially important because in some conditions the tail surfaces are completely immersed in the propeller wash, e.g., during hover on propeller thrust alone. Also, propeller slipstream flow curvature and propeller wash lag are critically important aerodynamics to capture. Second, the wing downwash is taken into account as well as ground effect aerodynamics through a downwash correction. Of course, an effect that must be modeled is the shielding or blanketing that occurs around the tail surfaces and in some situations promotes and sustains aircraft spin. While all of these effects
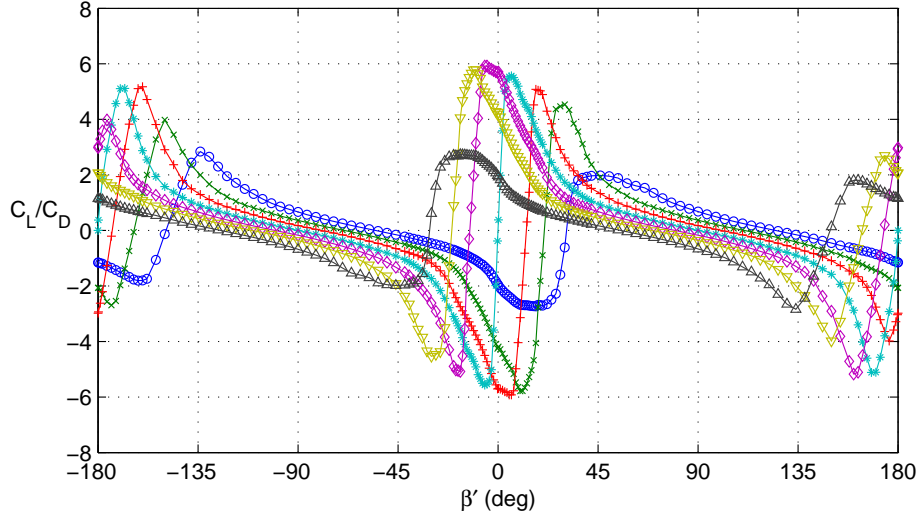
American Institute of Aeronautics and Astronautics

Figure 10. Vertical tail lift-to-drag characteristics over the full ±180-deg side angle of attack range for rudder deflections of 0, ±15, ±30, and ±50 deg (see Fig. 9 for legend).

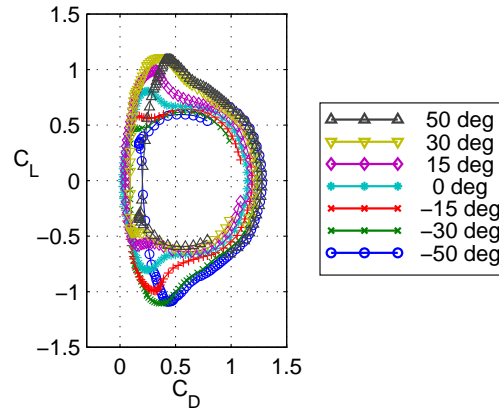**Figure 11. Vertical tail polar over the ±90-deg side angle of attack range for rudder deflections of 0, ±15, ±30, and ±50 deg.**

and others are modeled in the simulation, not all of these considerations are presented in this paper.

Typically tail surfaces have relatively low aspect ratios, and much data on such wings exists in the literature, some including flaps and high angle of attack data.[45–57] These references were used along with semi-empirical methods to construct full ±180 deg data. For the vertical fin of the ShowTime 50 model, the rudder control surface ratio S_r/S is 0.68, which is extreme (see Fig. 3). Using the methods developed for modeling such surfaces, the data shown in Figs. 9–11 was generated.

The propeller wash on the tail surface begins with the classic momentum theory result[58] that the flow through the propeller disc is given by

$$V_1 = V_\infty + w \tag{17}$$

where

$$w = \frac{1}{2}\left[-V_\infty + \sqrt{V_\infty^2 + \left(\frac{2T}{\rho A}\right)}\right] \tag{18}$$

There are a number of additional steps that are considered when extending this basic theory to flow at the tail in the general case of full-envelope flight which can include flight in yawed flow, unsteady aircraft motions,

American Institute of Aeronautics and Astronautics

wake lag effects, and propeller hover and steep descent conditions. These propeller effects are discussed in a separate companion paper.[26]

Wing downwash on the horizontal tail is modeled in realtime from the wing lift distribution and the geometry of the wing relative to the tail. From the lift distribution at any moment in time, the circulation distribution along the wing is determined. This vorticity is then shed into the wake as discrete filaments, that is, a system of horseshoe vortices that satisfy vortex continuity laws (Helmholtz theorem). The system includes vortices trailed from the wing tips and also inboard with alignment on aileron-flap junctures if they exist. Corrections are applied for wake contraction, angle of attack, sideslip, wall effect and others. These wake characteristics are then used to determine the downwash at each tail surface.

The aerodynamics of the tail surfaces can be strongly influenced by the surrounding surfaces when operating in high angle conditions. For instance, for a conventional tail surface arrangement in a 90-deg plunge, the vertical fin will not be exposed to the total relative flow velocity because the flow will be masked, or shielded, by the horizontal tail surface. In effect, the vertical fin in this case will be operating in the near stagnant "flow shadow" of the horizontal tail. For this case described, the effect is most dramatic for the 90-deg plunge, but it attenuates to zero as the angle of attack is reduced back to nominal cruise flight conditions. This effect is captured by a new approach described here.

Figure 12 shows the approach used in modeling this tail-surface shielding effect. The vertical fin for this aircraft operates in the flow shadow of the horizontal tail for off-nominal high angle conditions. A "flow shadow map" is constructed to model the fraction η_s relating the local relative flow to the total relative flow, that is

$$\eta_s = \frac{V_{R,\text{local}}}{V_{R,\text{total}}} \tag{19}$$

where $V_{R,\text{local}}$ is the flow exposed to the vertical fin, and $V_{R,\text{total}}$ is that determined from kinematics of the component. The fraction η_s ranges from zero (stagnant local flow) to 1 (no shielding present), and in this case for flow from below, η_s is functionally defined here as

$$\eta_s = f(\overline{u}, \overline{v}) \tag{20}$$

where $\overline{u}$ and $\overline{v}$ are the direction cosines for the total relative flow vector. Figure 13 shows the flow shadow map used to model this effect for the flow shadow on the vertical fin as a result of the horizontal tail beneath (case depicted in Fig. 12).

The flow shadow maps are used extensively to model shielding effects. For instance, for vertical fins that extend on either side of the horizontal tail shown in Fig. 3 are modeled by using two flow shadow maps – one as shown in Fig. 12 for the upper vertical fin and another for the lower vertical fin where flow from above is masked by the horizontal tail. Flow shadow maps are also used on the horizontal tail surfaces when flow is from the opposite side of the surface (captures shielding from the vertical fin and fuselage). Moreover, flow shadow maps are used on the inboard sections of the wing for flow from either side at high sideslip. For biplanes, flow shadow maps are used for each wing element to account for the shielding of one wing on the other. For aircraft with side force generators (see Fig. 3), flow maps are used much like that for the vertical fin with shielding from the horizontal tail. These maps in general are not axisymmetric, but instead sometimes squashed on one side depending on the local geometry that produces the shielding, or in some cases these flow shadow maps are 2D instead of 3D like Fig. 12. These maps are semi-empirical models that simulate the physics of the flow, but like many semi-empirical models (e.g., the myriad turbulence models with tunable parameters in CFD), these flow shadow maps that simulate the physics of the flow rely to some extent on tuning to produce results that mimic actual aircraft behaviors in high angle flight.

C. Fuselage Aerodynamics

Fuselage aerodynamics are modeled by dividing the fuselage into segments and determining the local relative flow which is then used together with the aerodynamic coefficients to yield the local forces which, as in all cases, are then resolved about the center of gravity. Figure 14 shows the ShowTime 50 side force lift coefficient for one panel for the full ± 180-deg side angle of attack β' range. The local flow is a summation of that from kinematics and wash models (propeller and downwash, including lag effects). Elements of the development rely on methods that have been used in missile aerodynamics; however, again no stability derivatives are applied.
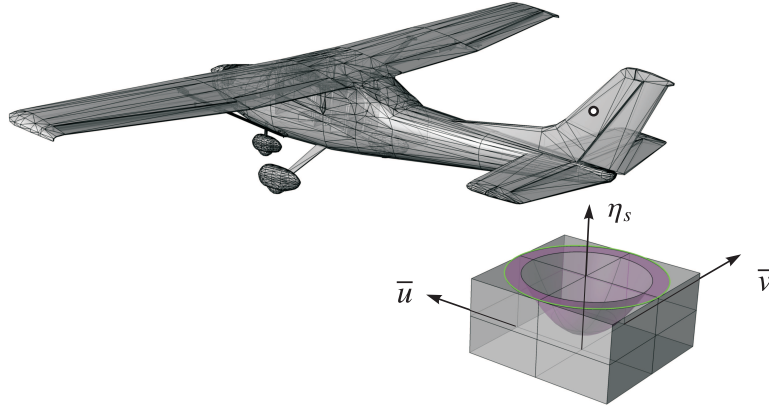
Figure 12. Flow shadow map approach used in modeling the shielding effect of the horizontal tail on the vertical fin for flow coming from beneath.
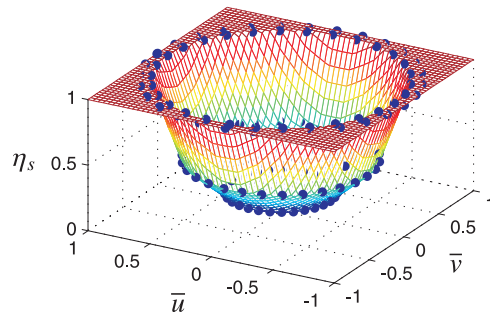

Figure 13. Flow shadow map data used in modeling the shielding effect of the horizontal tail on the vertical fin for flow coming from beneath for the Cessna 182 RC model.
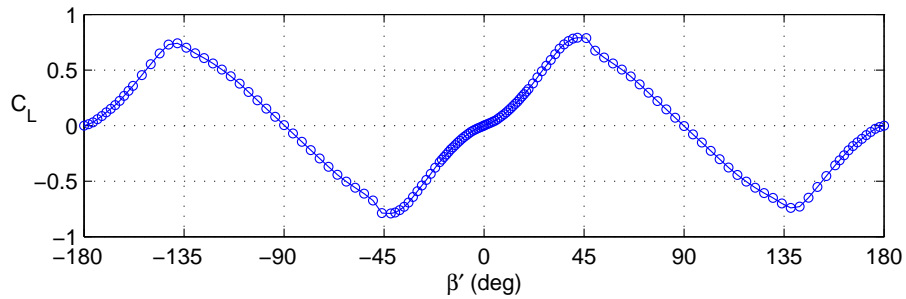

Figure 14. Fuselage side force lift coefficient over the full ± 180-deg side angle of attack range.

D.   Propeller Aerodynamics

Only a summary of the propeller force and moment modeling is included here while details are given in a companion paper.[26] For the normal working state (steady axial-flow conditions), the propeller thrust and torque are given by

$$T = \rho \, n^2 D^4 C_T \tag{21}$$

$$Q = \rho \, n^2 D^5 C_Q \tag{22}$$

where the thrust and torque coefficients are determined through lookup tables on the advance ratio given by

$$J = \frac{V_N}{n\,D} \tag{23}$$

In the method, the propeller thrust and torque coefficients are determined from blade element momentum theory, in particular, using the code PROPID.[59–61]

Apart from the basic propeller aerodynamics expressed in Eqs. 21 and 22, a number of other factors must be considered for any general motion and propeller attitude. These include propeller normal force and P-factor (yawing moment) when the flow is not axial, i.e. when the propeller is at an angle of attack to the flow. These effects are given by[58]

$$P_N = \frac{\sigma q A}{2}\left\{\overline{C}_l + \frac{aJ}{2\pi}\ln\left[1 + \left(\frac{\pi}{J}\right)^2\right] + \frac{\pi}{J}C_d\right\}\alpha \tag{24}$$

$$N_P = \frac{-\sigma q A R}{2}\left\{\frac{2\pi}{3J}\overline{C}_l + \frac{a}{2}\left[1 - \left(\frac{J}{\pi}\right)^2\ln\left(1 + \left[\frac{\pi}{J}\right]^2\right)\right] - \frac{\pi}{J}C_d\right\}\alpha \tag{25}$$

where the average lift coefficient $\overline{C}_l$ is expressed as

$$\overline{C}_l = \left(\frac{3J}{2\pi}\right)\left[\frac{2}{\sigma q A}\frac{J}{\pi}T + C_d\right] \tag{26}$$

A number of other significant and important propeller effects are modeled, such as propeller gyroscopic forces, aerodynamic moments from propeller wake swirl on downstream surfaces (wing, fuselage, and tail), propeller wash/tail surface damping effects, and propeller wash lag and wake curvature. The approach to modeling these effects is described in the companion paper.[26]

V. Simulation Framework and Validation

The full-envelope aerodynamics modeling methods as described are used in the flight simulator FS One.[25] The specific aircraft modeled in the simulator are shown in Table 1, and the same information in English units is given Table 2. The simulation solves the full 6-DOF equations of motion using quaternions, and integration is carried out using a Runge-Kutta 4-th order scheme running at 300 Hz on a desktop PC. An efficient interpolation method is incorporated into the code to the extent that upward of 250 tables can be interpolated in realtime while running the simulation at 300 Hz and rendering the graphics through a typical PC gaming graphics card at $\approx$100 Hz or better. The simulator allows for pilot control input through a standard RC transmitter, from any standard USB joystick or from a data file.

The code base is written in C++, is object oriented and includes approximately 600,000 lines of code together with 400,000 lines of code (various languages) for aero-physics model development. A large number of data files for aerodynamics, graphics, ground terrain elevation data, textures, etc. are read at runtime and make up a substantial part of the overall simulation framework and modeling. The simulator custom-physics engine includes collision detection algorithms between moving aircraft and ground-based objects. "Breakable-parts" physics are also modeled in the simulation to simulate crashes and subsequent missing-part flight dynamics. The simulator has a two-pilot mode where two pilots can fly on one PC using separate pilot controls and split-screen capabilities. Flight dynamics recording features are also embedded in the code to allow for saving state data to a file which can later be played back as a recording. Recordings can be played back as lessons or while actively flying in the simulator in either single-pilot or two-pilot mode.

Wind, the atmospheric boundary layer and turbulence are modeled using a full 3-D turbulent flowfield environment that captures lateral and longitudinal changes along the aircraft extent (wingtip-to-wingtip, nose-to-tail). Tabular turbulence data is generated a priori, read at runtime and used in realtime to obtain the turbulence quantities for all aircraft components. Also, slope winds and wind shear are modeled and used for slope soaring and dynamic soaring simulation.[62]

Table 1. Specifications for Airplanes Modeled in the FS One Flight Simulator (metric units).

Name	Category	b (m)	S (dm^2)	AR	l (m)	W (g)	W/S (g/dm^2)	Propulsion	Controls †
Aerobird	Beginner, Electric, ARF	1.40	20.83	9.371	1.05	1088.62	51.65	Electric/Propeller	TV(RE)
Alpha 40	Trainer, Glow, ARF	1.60	45.81	5.590	1.33	2617.23	56.50	Glow/Propeller	TRE2A
Ascent	Electric Glider, Beginner, ARF	1.37	21.35	8.810	0.83	553.38	25.57	Electric/Propeller	TRE
Bobcat	High Performance Jet	1.68	64.52	4.356	1.96	9634.30	147.53	Jet	T2R2E2A3GB
Brio	Aerobatic, 3D, Electric, ARF	1.04	20.97	5.172	1.02	802.86	37.93	Electric/Propeller	TRE2A
C-182	Scale, Gas, ARF	2.41	80.39	7.205	1.95	6903.68	84.85	Gas/Propeller	TRE2A2F
Corsair	Scale, Glow, Warbird, ARF	1.66	48.52	5.662	1.31	3633.27	74.02	Glow/Propeller	TRE2A
Edge 540	Aerobatic, Scale, IMAC/3D, Gas	2.48	111.68	5.492	2.16	10205.83	90.30	Gas/Propeller	TRE2A
Extra 260 EFL	Foamie, 3D, ARF	0.83	16.77	4.063	0.84	240.40	14.08	Electric/Propeller	TRE2A
F-22 PTS	PTS Trainer, Glow, ARF	1.32	47.16	3.699	1.28	3401.94	71.28	Glow/Propeller	TRE2A
Firebird	Beginner, Electric, ARF	1.00	11.03	9.069	0.76	453.59	40.58	Electric/Propeller	TE
Funtana 40	Aerobatic, 3D, Glow, ARF	1.42	46.06	4.392	1.42	2576.40	55.27	Glow/Propeller	TRE2A
Funtana 90	Aerobatic, 3D, Glow, ARF	1.77	71.47	4.360	1.74	3315.76	45.83	Glow/Propeller	TRE2A
J-3 Cub	Beginner, Electric, ARF	0.94	12.74	6.969	0.64	462.66	35.91	Electric/Propeller	TRE
J-3 Cub	Scale, Glow, ARF	2.03	59.29	6.964	1.27	3333.90	55.57	Glow/Propeller	TRE2A
MiG-15	Scale, High Performance Jet	1.73	61.68	4.837	1.73	9951.82	159.44	Jet	TRE2A3G2Ab
P-51 PTS	PTS Trainer, Glow, ARF	1.48	40.45	5.412	1.28	2898.46	73.63	Glow/Propeller	TRE2A
P-51	Scale, Glow, Warbird, ARF	1.96	67.03	5.706	1.73	6681.42	98.51	Glow/Propeller	TRE2A2F
Pawnee	Scale, Glow, Towplane	3.22	134.19	7.706	2.29	12786.77	94.13	Glow/Propeller	TRE2A2F
Showtime 50	Aerobatic, 3D, Gas, ARF	1.45	46.58	4.500	1.51	2902.99	61.54	Gas/Propeller	TRE2A
Showtime 50 SFG	Aerobatic, 3D, Gas, ARF	1.45	46.58	4.500	1.51	3025.46	64.22	Gas/Propeller	TRE2A
Slo-V	Beginner, Electric, ARF	1.17	31.55	4.327	0.93	458.13	14.35	Electric/Propeller	TV(RE)
Stryker	Sport, Electric, ARF	0.94	23.29	3.792	0.69	562.45	23.85	Electric/Propeller	T2Elv
Supra	Sailplane, Thermal/Duration	3.40	67.87	17.068	1.73	1855.19	27.05		TRE2A2F
Swift	Scale, Sailplane	5.54	228.54	13.428	2.96	14514.96	62.75		RE2A2SG
T-34	Scale, Glow, Warbird, ARF	1.45	35.81	5.906	1.14	2921.13	80.66	Glow/Propeller	TRE2A2G
Texan	Scale, Glow, Warbird, ARF	1.71	45.55	6.454	1.22	3506.27	76.07	Glow/Propeller	TRE2A2G
Tracon	Sailplane, Thermal/Duration	3.15	58.82	16.892	1.31	2077.45	34.95		RE2A2F
Tribute	Foamie, 3D, ARF	0.94	24.17	3.654	0.95	403.70	16.46	Electric/Propeller	TRE2A
Twist	Aerobatic, 3D, Glow, ARF	1.21	48.22	3.051	1.23	2485.69	50.96	Glow/Propeller	TRE2A
Ultimate EFL	Foamie, 3D, ARF	0.71	24.84	2.036	0.75	403.70	16.13	Electric/Propeller	TRE4A
Ultimate TOC	Aerobatic, Scale, IMAC/3D	2.54	213.55	3.021	2.79	18170.91	84.06	Gas/Propeller	TRE4A
Ultra Stick Lite	Sport, Gas	1.93	79.35	4.696	1.40	4522.32	56.32	Gas/Propeller	TRE2A2F

† Key for controls: T = throttle, R = rudder, E = Elevator, A = ailerons, F = flaps, S = spoilers, Ab = airbrakes, G = landing gear, B = wheel brakes, V = V-tail, Elv = elevons. An index preceding a control indicates number of independent controls, e.g. "2A" means two ailerons independently controlled through mixing.

Table 2. Specifications for Airplanes Modeled in the FS One Flight Simulator (English units).

Name	Category	b (in)	S (in^2)	AR	l (in)	W (lb)	W/S (oz/ft^2)	Propulsion	Controls †
Aerobird	Beginner, Electric, ARF	55.00	322.80	9.371	41.50	2.40	17.13	Electric/Propeller	TV(RE)
Alpha 40	Trainer, Glow, ARF	63.00	710.00	5.590	52.50	5.77	18.74	Glow/Propeller	TRE2A
Ascent	Electric Glider, Beginner, ARF	54.00	331.00	8.810	32.50	1.22	8.48	Electric/Propeller	TRE
Bobcat	High Performance Jet	66.00	1000.00	4.356	77.00	21.24	48.93	Jet	T2R2E2A3GB
Brio	Aerobatic, 3D, Electric, ARF	41.00	325.00	5.172	40.00	1.77	12.58	Electric/Propeller	TRE2A
C-182	Scale, Gas, ARF	94.75	1246.00	7.205	76.75	15.22	28.14	Gas/Propeller	TRE2A2F
Corsair	Scale, Glow, Warbird, ARF	65.25	752.00	5.662	51.50	8.01	24.55	Glow/Propeller	TRE2A
Edge 540	Aerobatic, Scale, IMAC/3D, Gas	97.50	1731.00	5.492	85.00	22.50	29.95	Gas/Propeller	TRE2A
Extra 260 EFL	Foamie, 3D, ARF	32.50	260.00	4.063	33.00	0.53	4.67	Electric/Propeller	TRE2A
F-22 PTS	PTS Trainer, Glow, ARF	52.00	731.00	3.699	50.30	7.50	23.64	Glow/Propeller	TRE2A
Firebird	Beginner, Electric, ARF	39.38	171.00	9.069	30.00	1.00	13.46	Electric/Propeller	TE
Funtana 40	Aerobatic, 3D, Glow, ARF	56.00	714.00	4.392	56.00	5.68	18.33	Glow/Propeller	TRE2A
Funtana 90	Aerobatic, 3D, Glow, ARF	69.50	1107.80	4.360	68.50	7.31	15.20	Glow/Propeller	TRE2A
J-3 Cub	Beginner, Electric, ARF	37.10	197.50	6.969	25.00	1.02	11.91	Electric/Propeller	TRE
J-3 Cub	Scale, Glow, ARF	80.00	919.00	6.964	49.90	7.35	18.43	Glow/Propeller	TRE2A
MiG-15	Scale, High Performance Jet	68.00	956.00	4.837	68.00	21.94	52.88	Jet	TRE2A3G2Ab
P-51 PTS	PTS Trainer, Glow, ARF	58.25	627.00	5.412	50.50	6.39	24.42	Glow/Propeller	TRE2A
P-51	Scale, Glow, Warbird, ARF	77.00	1039.00	5.706	68.00	14.73	32.67	Glow/Propeller	TRE2A2F
Pawnee	Scale, Glow, Towplane	126.60	2080.00	7.706	90.00	28.19	31.22	Glow/Propeller	TRE2A2F
Showtime 50	Aerobatic, 3D, Gas, ARF	57.00	722.00	4.500	59.50	6.40	20.41	Gas/Propeller	TRE2A
Showtime 50 SFG	Aerobatic, 3D, Gas, ARF	57.00	722.00	4.500	59.50	6.67	21.30	Gas/Propeller	TRE2A
Slo-V	Beginner, Electric, ARF	46.00	489.00	4.327	36.75	1.01	4.76	Electric/Propeller	TV(RE)
Stryker	Sport, Electric, ARF	37.00	361.00	3.792	27.00	1.24	7.91	Electric/Propeller	T2Elv
Supra	Sailplane, Thermal/Duration	134.00	1052.00	17.068	68.20	4.09	8.97		TRE2A2F
Swift	Scale, Sailplane	218.10	3542.40	13.428	116.70	32.00	20.81		RE2A2SG
T-34	Scale, Glow, Warbird, ARF	57.25	555.00	5.906	45.00	6.44	26.75	Glow/Propeller	TRE2A2G
Texan	Scale, Glow, Warbird, ARF	67.50	706.00	6.454	48.00	7.73	25.23	Glow/Propeller	TRE2A2G
Tracon	Sailplane, Thermal/Duration	124.10	911.70	16.892	51.40	4.58	11.59		RE2A2F
Tribute	Foamie, 3D, ARF	37.00	374.62	3.654	37.50	0.89	5.46	Electric/Propeller	TRE2A
Twist	Aerobatic, 3D, Glow, ARF	47.75	747.37	3.051	48.38	5.48	16.90	Glow/Propeller	TRE2A
Ultimate EFL	Foamie, 3D, ARF	28.00	385.00	2.036	29.50	0.89	5.35	Electric/Propeller	TRE4A
Ultimate TOC	Aerobatic, Scale, IMAC/3D	100.00	3310.00	3.021	110.00	40.06	27.88	Gas/Propeller	TRE4A
Ultra Stick Lite	Sport, Gas	76.00	1230.00	4.696	55.00	9.97	18.68	Gas/Propeller	TRE2A2F

† Key for controls: T = throttle, R = rudder, E = Elevator, A = ailerons, F = flaps, S = spoilers, Ab = airbrakes, G = landing gear, B = wheel brakes, V = V-tail, Elv = elevons. An index preceding a control indicates number of independent controls, e.g. "2A" means two ailerons independently controlled through mixing.
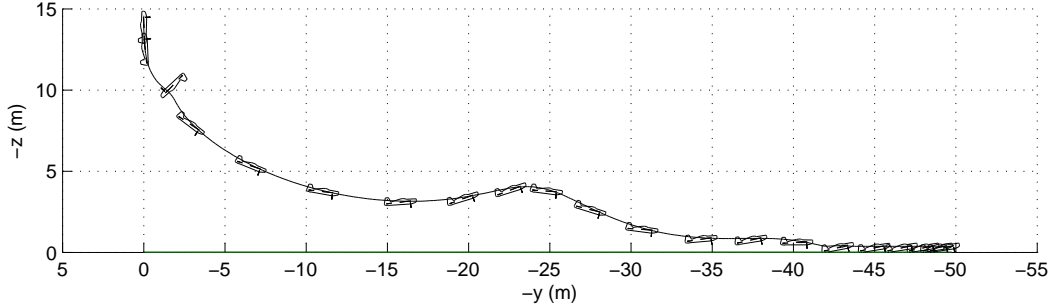
Figure 15. Trajectory of the Extra 260 EFL aerobatic aircraft performing a tailslide [aircraft magnified 2.5 times normal size and drawn every 0.55 sec, wingspan of 826 mm (32.5 in)].

The framework described here is the beginning of a new capability for simulation and modeling of full-envelope aircraft flight dynamics. The validation of the approach relies on the validation of the aerodynamics subsystem component models, which has been accomplished step-by-step for most components described. However, as with any simulation environment, especially in this case involving full-envelope modeling, elements of the simulation must depend to some extent on tuning of parameters to mimic known flight behaviors. Any tuning must result in prescribed data that remains within reasonable physical bounds, such as the approach used here to model the shielding effects at high angles. Where tuning of physical models is used, any of these methods are candidates for refinement by other means as new capabilities become available, e.g. when it is economical to simulate in CFD defined spin states that could be used to advance models for use in realtime simulations. Finally, in the development of the approach, over 30 aircraft were modeled, and in many cases field tests were performed, recorded on video and used in tuning and refining the methods. Moreover, every airplane in the simulator and hence its underlying models were tested by professional RC pilots (many having more than 30 yrs experience in flying RC models at all levels). The comments by the pilots were in sum that the simulation was very realistic across the broad range of models simulated.

VI. Simulations and Discussion

In this section, flight simulation results of four airplanes performing aerobatic-type maneuvers are discussed. The maneuvers are briefly described using the flight path trajectory and aircraft state data time histories. Superimposed on the trajectory is a skeleton outline of the aircraft oriented accordingly, and the ground trace is shown as a green line. Although the flight dynamics is carried out at 300 Hz, the time history data is plotted at a rate of 30 Hz, which is the recording rate used for these flights. For several of the flights described, the maneuver is complex and difficult to ascertain based on these short descriptions and graphics alone. In these cases, videos of these flights can be viewed online.[‡] All of the flights presented here were performed by the author, and the results are consistent with observations.

A. Tailslide

The first simulation is a tailslide of the Extra 260 (shown Fig. 1) in longitudinal flight with no control inputs used, and the propeller is static for the duration of the flight. The initial aircraft pitch angle θ is 92 deg, the angle of attack is -178 deg, and the aircraft begins at rest. Figure 15 shows the resulting trajectory in the y-z plane, and Fig. 16 shows the corresponding time history. As noted in the figure caption, the aircraft is rendered at 2.5 times normal size, and it is drawn every 0.55 sec in this particular case. As the airplane begins to slide, it is statically unstable in this direction of flight, and thus the nose begins to pitch towards the ground (positive q). After 1 sec the airplane flips around nose first. When this happens the following rapidly occurs: pitch rate peaks, airspeed dips, pitch angle passes through -90 deg and the angle of attack reaches a positive value. Thereafter the gliding airplane zooms and enters the phugoid mode where the angle of attack approaches nearly a constant value before landing.

[‡]All simulated flights were recorded as videos and are available online at `http://www.ae.illinois.edu/m-selig/animations`.

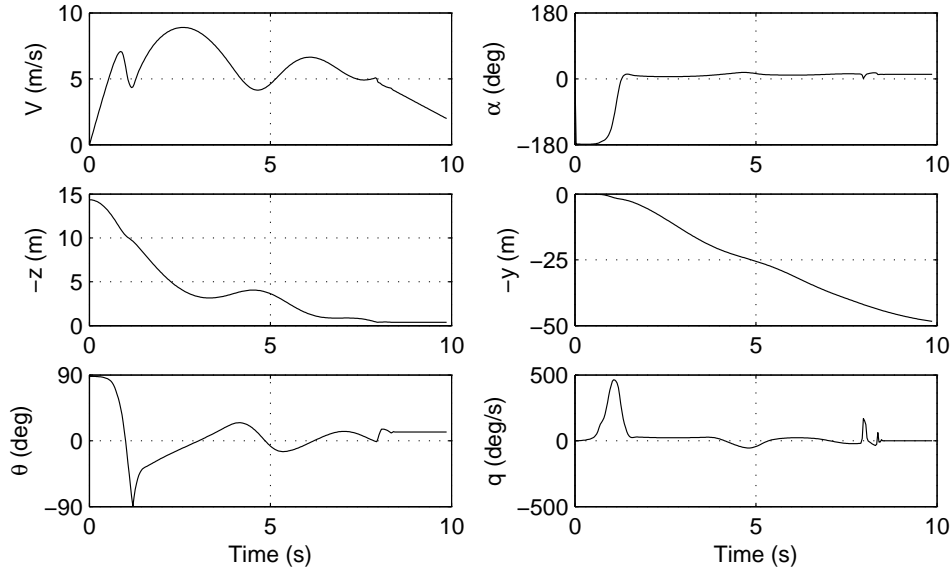American Institute of Aeronautics and Astronautics

Figure 16. Time history of the Extra 260 EFL aerobatic aircraft performing a tailslide (see Fig. 15 for trajectory).

B. Tailslide with Aileron Input

This next case is the same as before except full left-aileron input (which is opposite that shown in Fig. 1) is used and held constant for the flight. Also, the initial pitch angle is 90 deg. With the flow directly from behind, the initial angle of attack is 180 deg, and as the airplane falls the flow moves past the 180 deg to −180 deg before flipping around and flying in forward flight. As would be expected, the aircraft in the tailslide first rolls right (positive p) due to reverse flow on the wing, and then after turning around nose first it rolls left (negative p) as shown in Figs. 17 and 18. When the airplane is released, the initial sideslip angle begins from a value of 180 deg (relative wind is "in the left ear"), and this value is used in the aerodynamics calculations. The time history, however, does not show this because the angle plotted is taken from the aircraft state where it is defined per convention to be $\beta = \arcsin(v/V)$ which is always limited to ±90 deg.

C. Knife Edge Flight

The ShowTime 50 aircraft can be configured with or without wing side force generators (see Fig. 3). With the side force generators (SFGs) knife edge flight is enhanced, and this increased performance can be shown in simulation. Figures 19 and 20 are for the ShowTime 50 without SFGs entering a roll and thereafter sustaining knife edge flight with largely right-rudder input. The rudder input is held constant until eventually the fuselage stalls in knife edge flight, reaching a sideslip angle of near −65 deg, and rudder input is relieved near 5.5 sec. These same inputs (though truncated in time) were used for the configuration with SFGs, and the results are shown in Figs. 21 and 22. With SFGs, the aircraft climbs in knife edge flight and initiates a knifed edge loop.

D. High Angle of Attack Flight – Harrier

With thrust-to-weight ratios of 2:1, slow flight under power at high angle of attack in the post-stall regime is possible. In model aviation, this aerobatic maneuver is called a "harrier." Figures 23 and 24 show a long quasi-steady flight that circles tighter and tighter to a center point where the horizontal speed is ultimately arrested, terminating in a vertical exit at the center of the spiral. The aircraft is the 33%-scale Edge 540 listed in Table 1 and sketched in Fig. 2.

    The flight begins in normal cruise with the angle of attack near 10 deg. As time goes on the up-elevator input is continuously increased. At around 30 sec into the flight, the throttle is advanced because
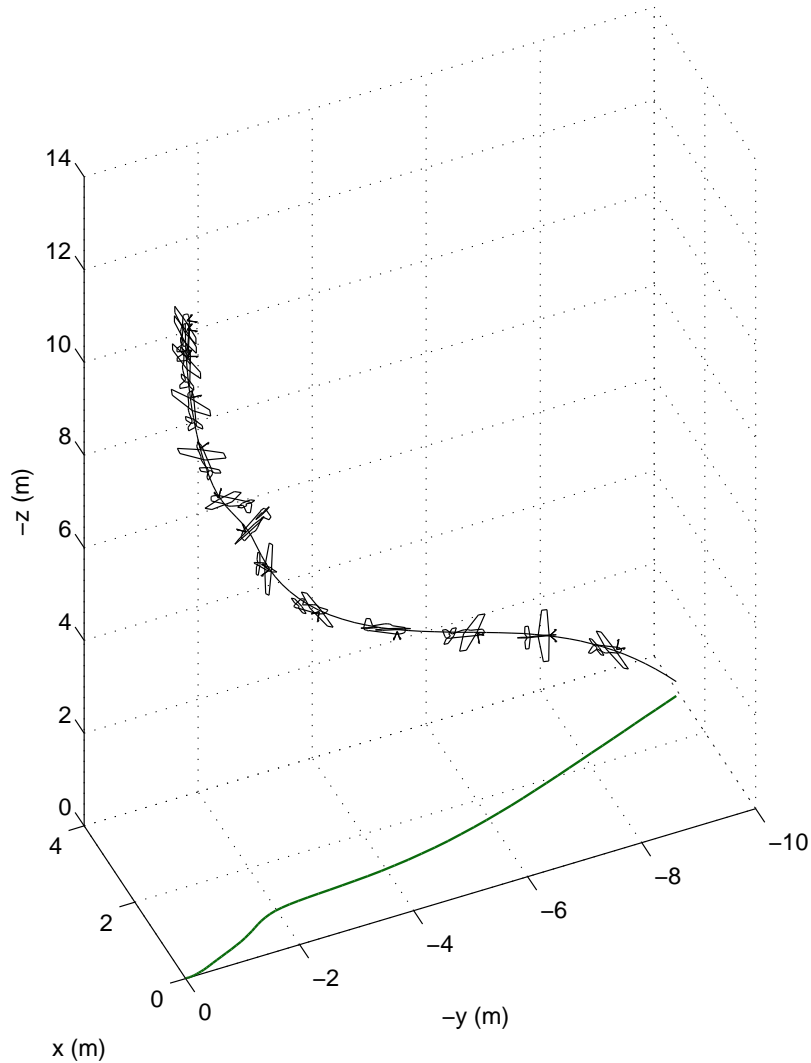
Figure 17. Trajectory of the Extra 260 EFL aerobatic aircraft performing a tailslide with full left aileron input [aircraft normal size and drawn every 0.2 sec, wingspan of 826 mm (32.5 in)].

the airplane passes from normal flight into the high-drag post-stall regime (around an angle of attack of 20 deg). Advancing throttle is required to maintain a height just above ground level. As the flight continues, up-elevator input is increased, the pitch increases, the flight speeds slows, and the throttle is advanced to counter the increasing drag and loss in wing lift. The resulting slow flight and high pitch are the distinctive hallmarks of a harrier maneuver. This result can be seen in the trajectory where the the pitch increases and the airplane slows (shorter spacing between aircraft plotted at a time interval of 2 sec). At the center of the spiral the airplane is ultimately slowed to a hover position and pointed straight up before advancing the throttle and climbing out (increasing $-z$).

E. Upright and Inverted Harrier Sequence

Harriers can be performed upright or inverted, and Figs. 25 and 26 show a flight that includes both for the Edge 540. Apart from the climbing roll at 12 sec (at $-y \approx -50$ m in Fig. 25), the aircraft is upright until approximately 27 sec into the flight (at $-y \approx 50$ m) when the airplane rolls inverted. The transition can be seen in the angle of attack going from positive to negative and the elevator deflection changing from up elevator to down elevator, which maintains the harrier high angle of attack. What is worth noting are the

American Institute of Aeronautics and Astronautics
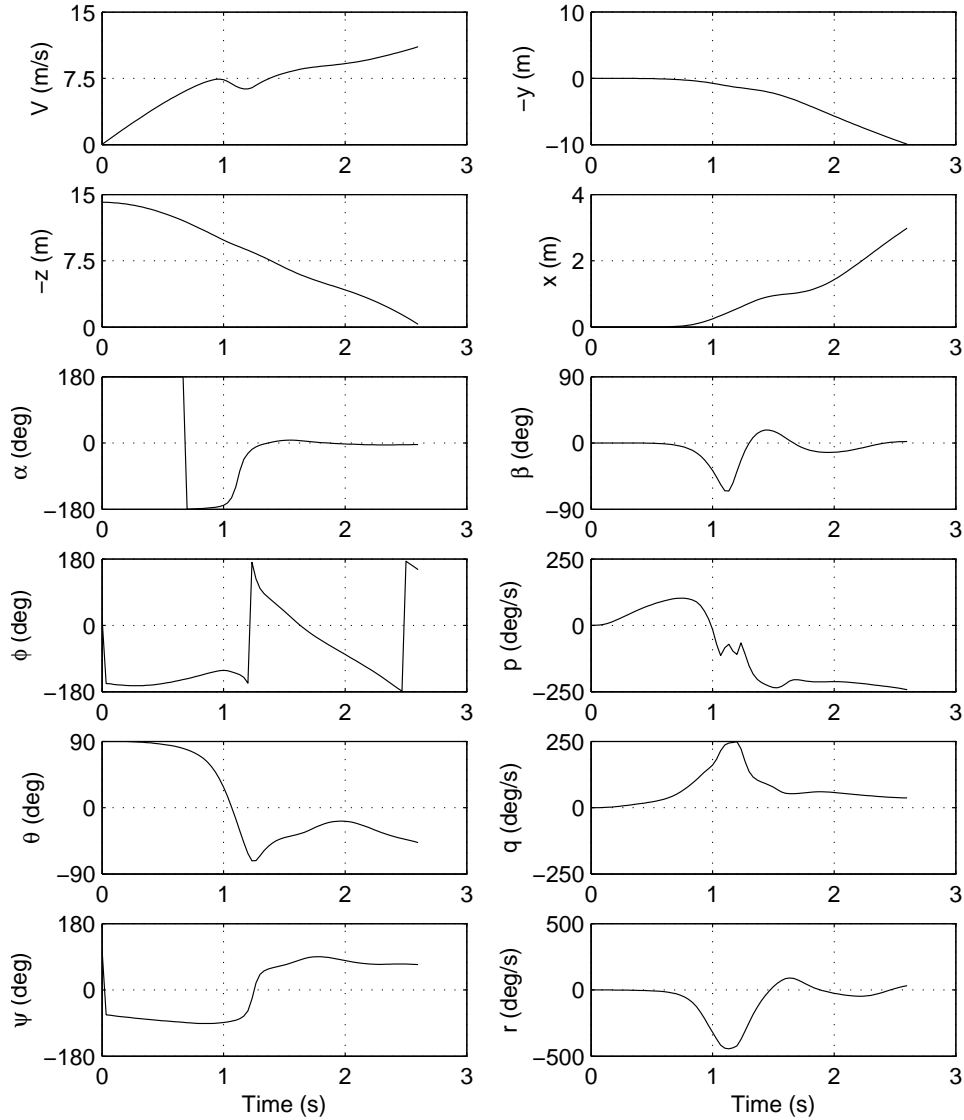
Figure 18. Time history of the Extra 260 EFL aerobatic aircraft performing a tailslide with full left aileron input (see Fig. 17 for trajectory).

accelerations (changes) in roll, pitch, and yaw rates. When upright for the first ≈27 deg, the aircraft is more unsteady and difficult to fly; whereas, when inverted the excursions are reduced. In real observations, upright harrier flight of model-scale aircraft are known to wing rock,[34] and this characteristic is partly captured by the simulation as demonstrated here in the time histories.

F.   Rolling Harriers

As it sounds, rolling harriers involve rolling flight at slow speeds while maintaining a high angle. The roll is achieved with constant aileron deflection, while the high angle is supported by modulating elevator and rudder input out-of-phase once per roll. As an example, for a left roll, up elevator is used when upright, followed by right rudder when in knife edge. As the roll continues into an inverted attitude, down elevator is used followed by left rudder when in knife edge. The cycle continues for each harrier roll.

Rolling harriers were simulated using the 46%-scale Ultimate TOC biplane shown in Fig. 27 (see Table 1). Figures 28 and 29 show the rolling harrier maneuver. After takeoff, the left roll starts at 4 sec and ends at

American Institute of Aeronautics and Astronautics
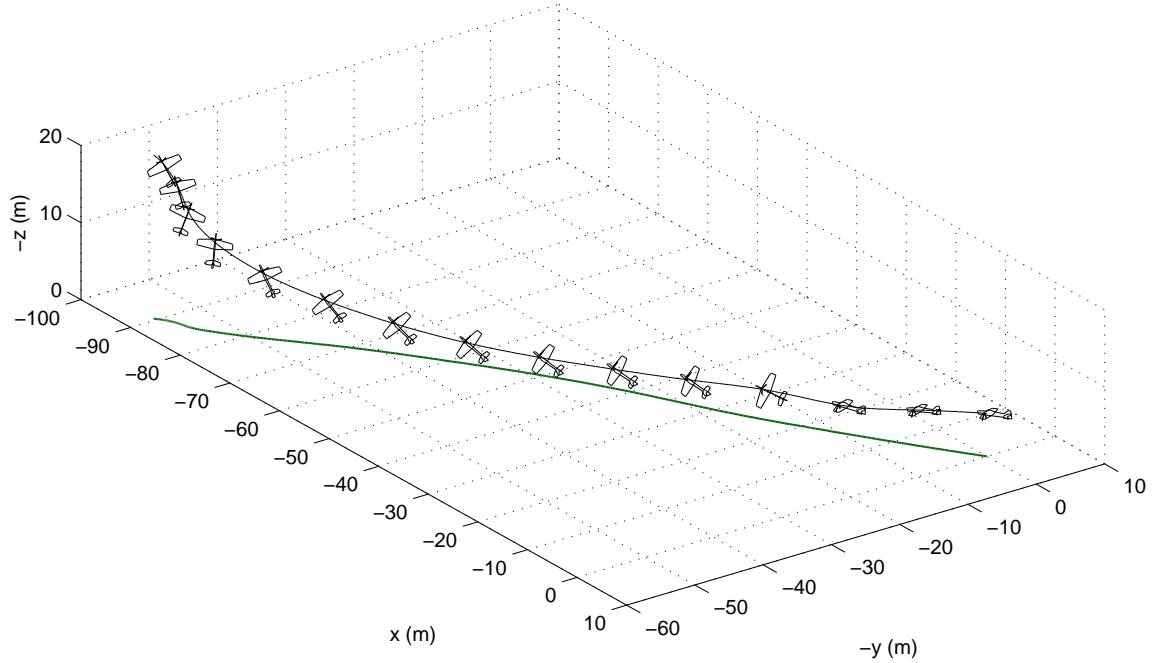
Figure 19. Trajectory of the ShowTime 50 aerobatic aircraft in knife edge flight [aircraft magnified 3 times normal size and drawn every 0.5 sec, wingspan of 1448 mm (57 in)].

17 sec as seen in the time history of the roll rate p. During this period of time the aileron input is constant to maintain the constant roll. The high angle is seen in the time histories of the angle of attack and sideslip. These angles modulate out of phase because for the most part the roll is axial with positive pitch θ. To sustain the high angle, the elevator and rudder are modulated out of phase as seen in their time histories. During the turning part of the trajectory near 10 sec into the flight, the elevator and rudder inputs are modulated not only out of phase but also biased to the roll angle so that the airplane is turned by their inputs. Of course, this is difficult to see from the time histories, but in video animation the effect is clearly visible. One subtle effect are the slight undulations in the elevation z during the roll. These undulations are caused by the aircraft falling through the knife edge phases of flight while climbing up during the upright and inverted harriers phases of the roll. Some skilled professional aerobatic pilots notice this effect and synchronize throttle burst inputs with the knife edge phases to climb at those points and thus maintain a more constant elevation and thus a more perfect maneuver for visual effect. Finally, it is interesting to see the total harrier angle (angle of attack and sideslip) start small, grow and then decay. This result is a function of the total net pilot input (elevator and rudder) that is producing the motion.

G. Inverted Spin – The Blender

The final example here exercises the edges of the aerobatic envelope – the inverted spin. In particular, the entire vertical maneuver from start-to-finish is called the blender, shown in Figs. 30 and 31. From a high altitude (≈ 340 m) the Ultimate TOC begins a nose down attitude and accelerates along the vertical line at near 90-deg pitch angle (θ). At 5.7 sec into the flight, a left-aileron pulse input produces a rapid roll rate (p). A fraction of a second after this point, at 6.2 sec, rapid down elevator and right-rudder input cause the airplane to pitch inverted (negative q, increasing θ) and yaw. At this point, the energy in the angular momentum that was focused around the roll axis (x) is transfer to angular momentum around the yaw axis (z). In the process the total angular momentum is more or less conserved. At just the point where the transition begins (starts at 6.2 sec), the visual effect is dramatic with the airplane yaw rate peaking and the pitch attitude flattening. Starting at 6.7 sec the aileron input is relieved while the elevator and rudder input are maintained. The airplane then settles into a steady slow-descent inverted spin at idle throttle setting. As the airplane spins, the heading (ψ) changes continuously at a nearly constant rate – 1.46 sec per rotation.
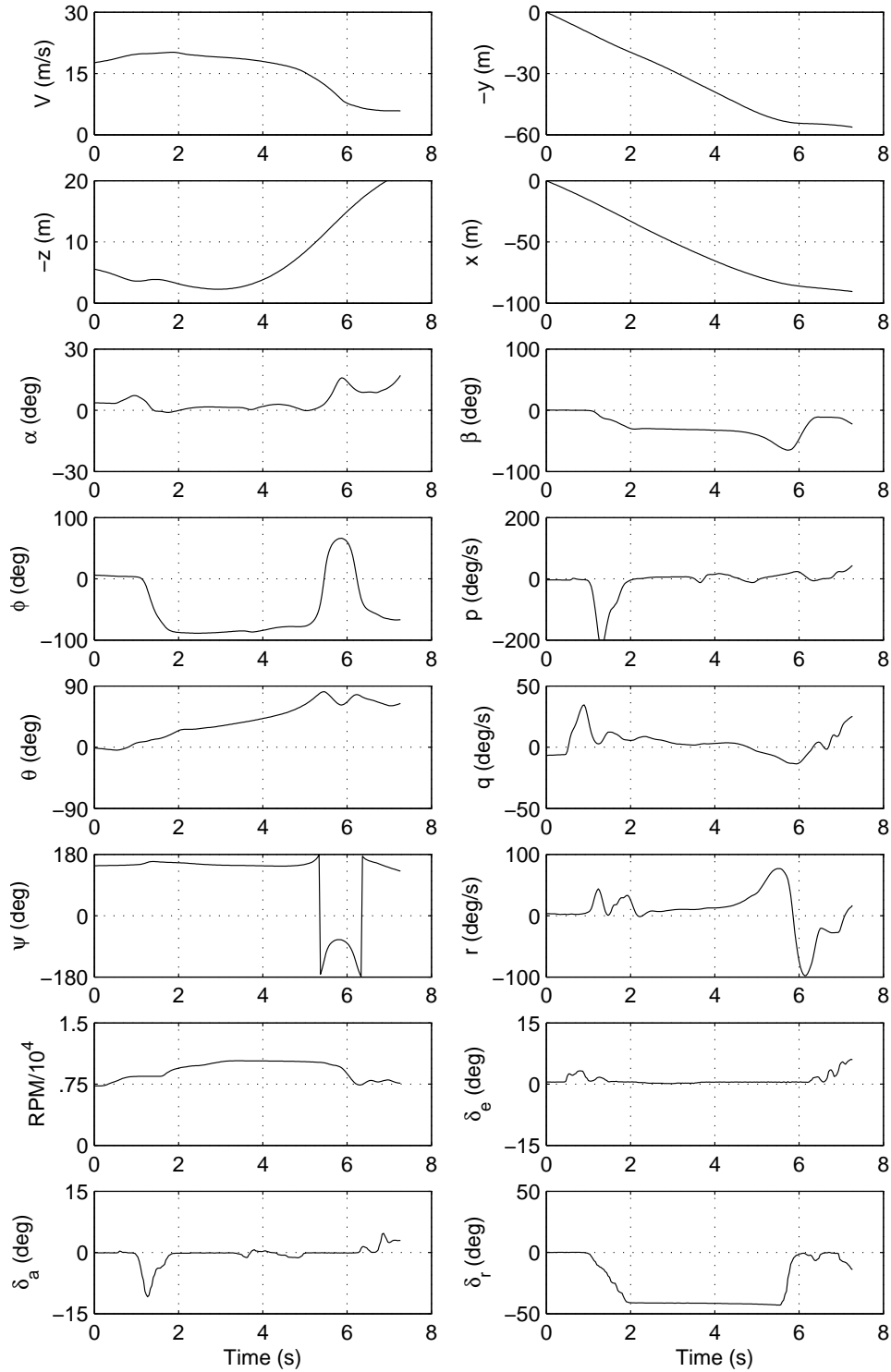
American Institute of Aeronautics and Astronautics

Figure 20. Time history of the ShowTime 50 aerobatic aircraft in knife edge flight (see Fig. 19 for trajectory).

The periodicity can also be seen in the trajectory (Fig. 30) where the interval between aircraft renderings is 0.365 sec, or once every 90 deg of spin rotation. Once the steady spin develops, the ground trace (green line in Fig. 30) is nearly circular, and the changes in x and y time histories are thus sinusoidal (see Fig. 31).
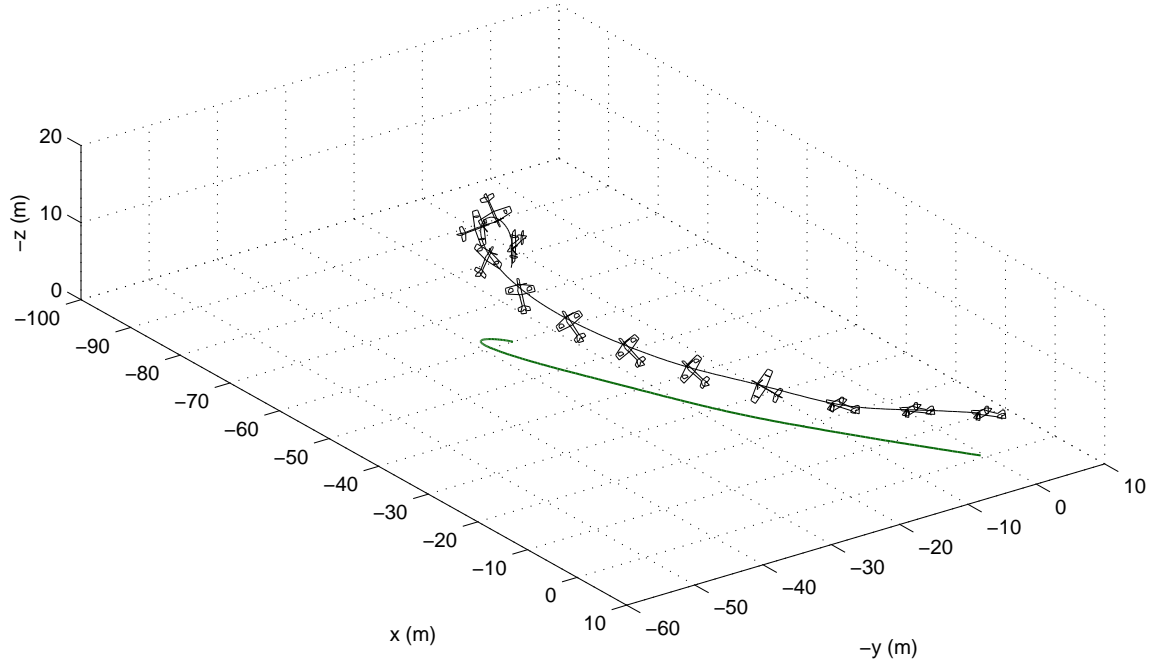
American Institute of Aeronautics and Astronautics

Figure 21. Trajectory of the ShowTime 50 SFG aerobatic aircraft in knife edge flight with same input as that use in Fig. 19 [aircraft magnified 3 times normal size and drawn every 0.5 sec, wingspan of 1448 mm (57 in)].

Termination of the downline spin begins at 20 sec where rudder input is released followed by advancing throttle, then corrective opposite aileron input and finally nose-up elevator input before flaring to land at the pilot station.

VII.   Conclusion

This paper shows that complex aerobatic full-envelope maneuvers performed by small ultra-agile RC/UAV configurations can be simulated using ±180 deg high-angle data in the component-based approach described here. The wings, tail, fuselage, etc. are all modeled separately with corrections applied for any interactions. To capture wide excursions that can occur along the span of the wing, such as in a spin, each wing is subdivided into sections and modeled individually, taking into account appropriate downwash effects. It is believed that this strip theory approach is most likely the best way to capture myriad complex nonlinear aerodynamic effects in realtime fixed-wing aircraft simulations, and the approximation has many avenues for advancement. The tail surfaces are modeled separately, e.g. right horizontal tail, left horizontal tail, etc. However, each tail surface component is not subdivided using a lifting-line theory approach but rather modeled as a full surface. No stability derivatives are used because it is believed that such an approach is not amenable to modeling ±180 deg high-angle flight. Rather full aerodynamic coefficients (e.g. $C_l, C_d, \ldots, C_L, C_D, \ldots$) are used. A key element of the current approach involves calculating the local relative flow that takes into account all effects – flight speed, kinematics of the aircraft rotation motions, propeller wash, downwash, and any shielding effects of one surface on another. New approaches to predicting local airfoil section data at high angle with large control surface deflections are also believed to be key in the success of the method, but these details are not included in the current paper. This approach in aggregate is able to model challenging problems in aerodynamics and flight dynamics, including aircraft spin, e.g. as was shown here – the inverted spin of a biplane configuration. The validity of the approach relies on the validity of each sub-model making up the entire aerodynamics model, and the final results of the simulations are consistent with recorded video observations and pilot experience. The approach is readily extended to aircraft of any size, e.g. the approach has been used to model spin and aerobatic maneuvers of full-scale aircraft. Moreover, the generality of the approach has been applied to model aircraft with missing, damaged or inoperative parts.

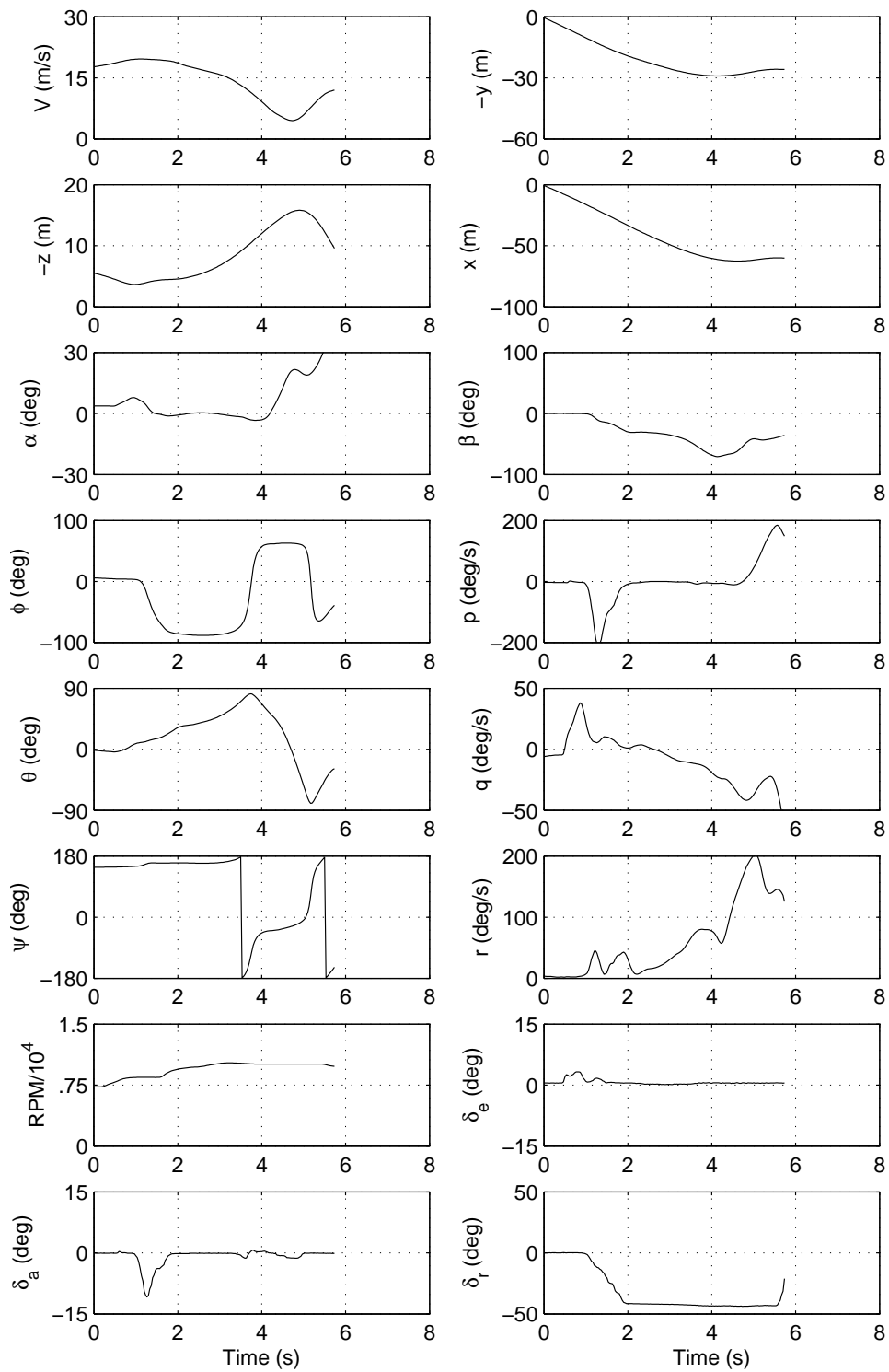American Institute of Aeronautics and Astronautics

Figure 22. Time history of the ShowTime 50 SFG aerobatic aircraft in knife edge flight with same input as that use in Fig. 19 (see Fig. 21 for trajectory).

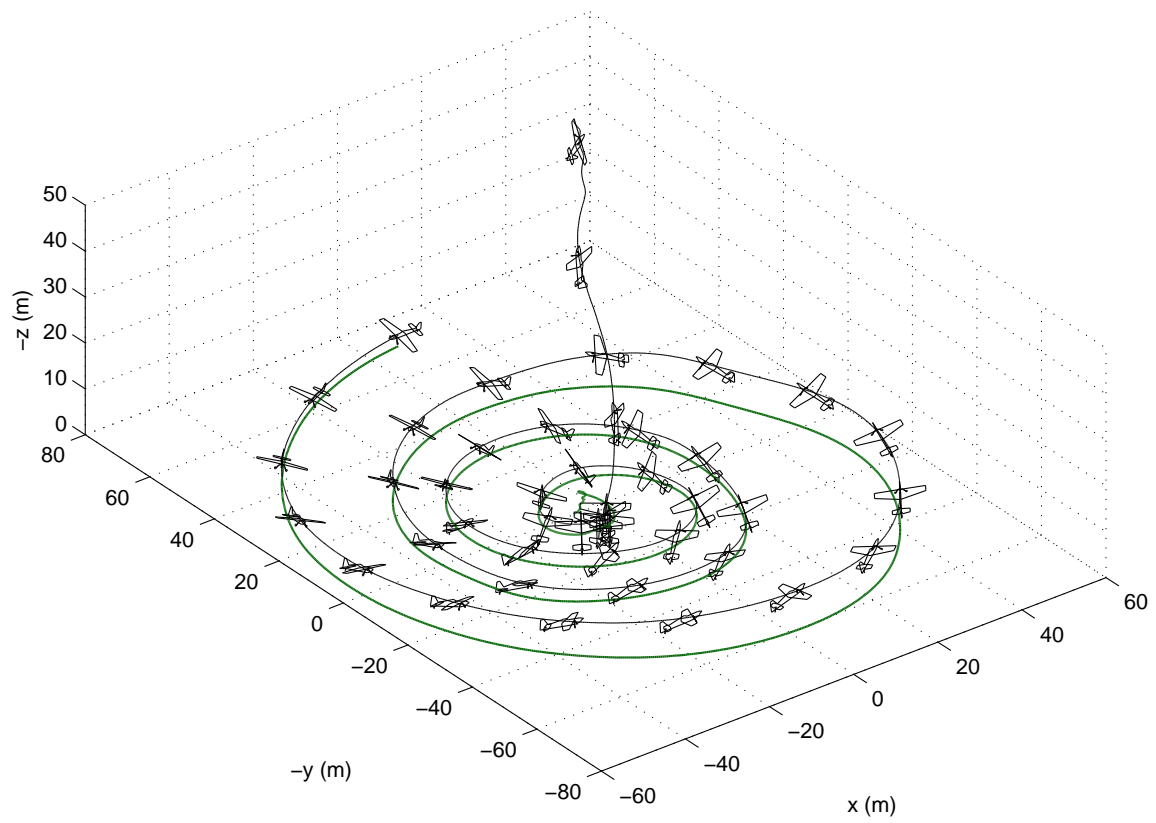American Institute of Aeronautics and Astronautics

Figure 23. Trajectory of the 33%-scale Edge 540 aerobatic aircraft in a high angle of attack harrier [aircraft magnified 4 times normal size and drawn every 2 sec, wingspan of 2476.5 mm (97.5 in)].
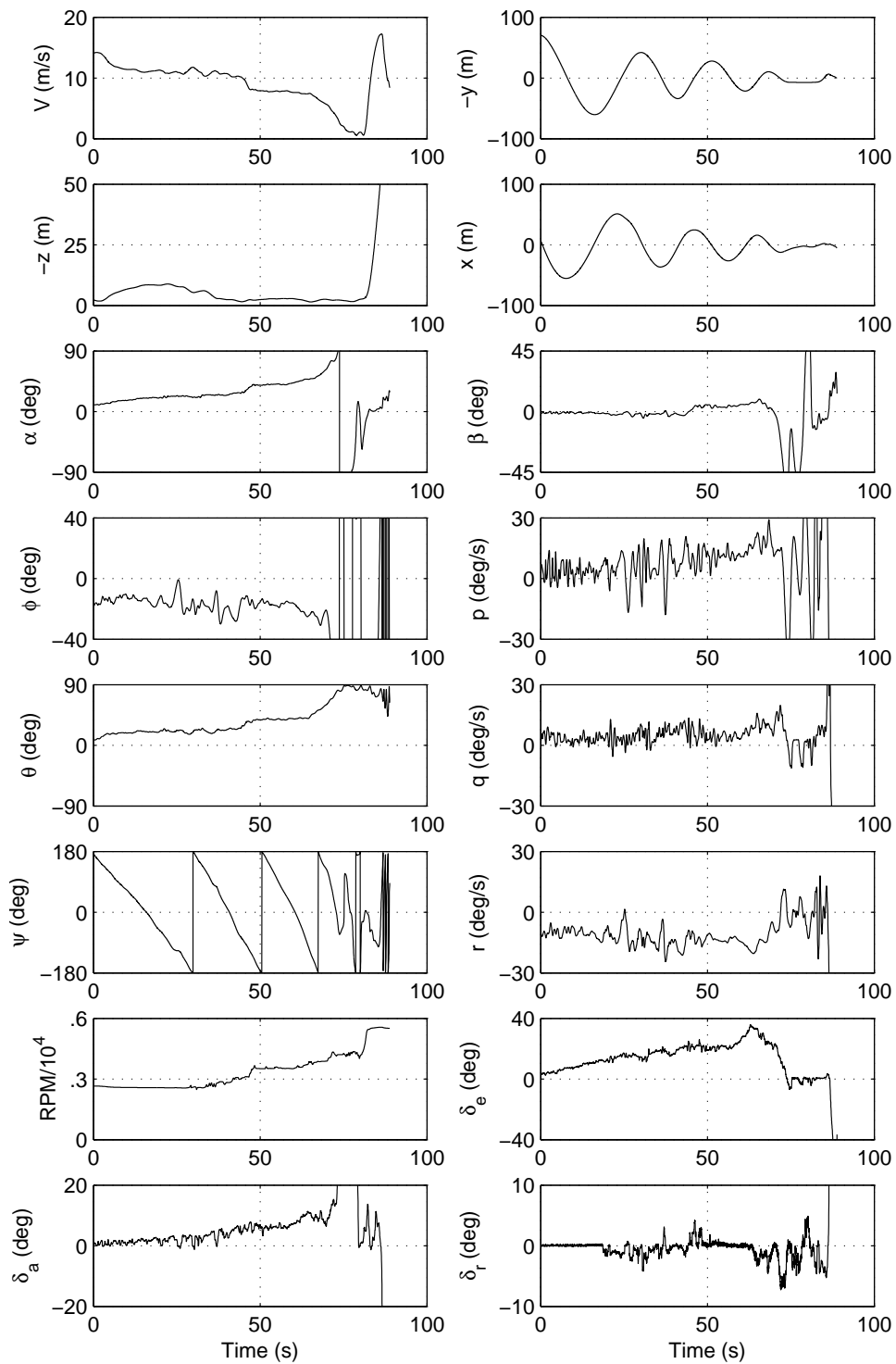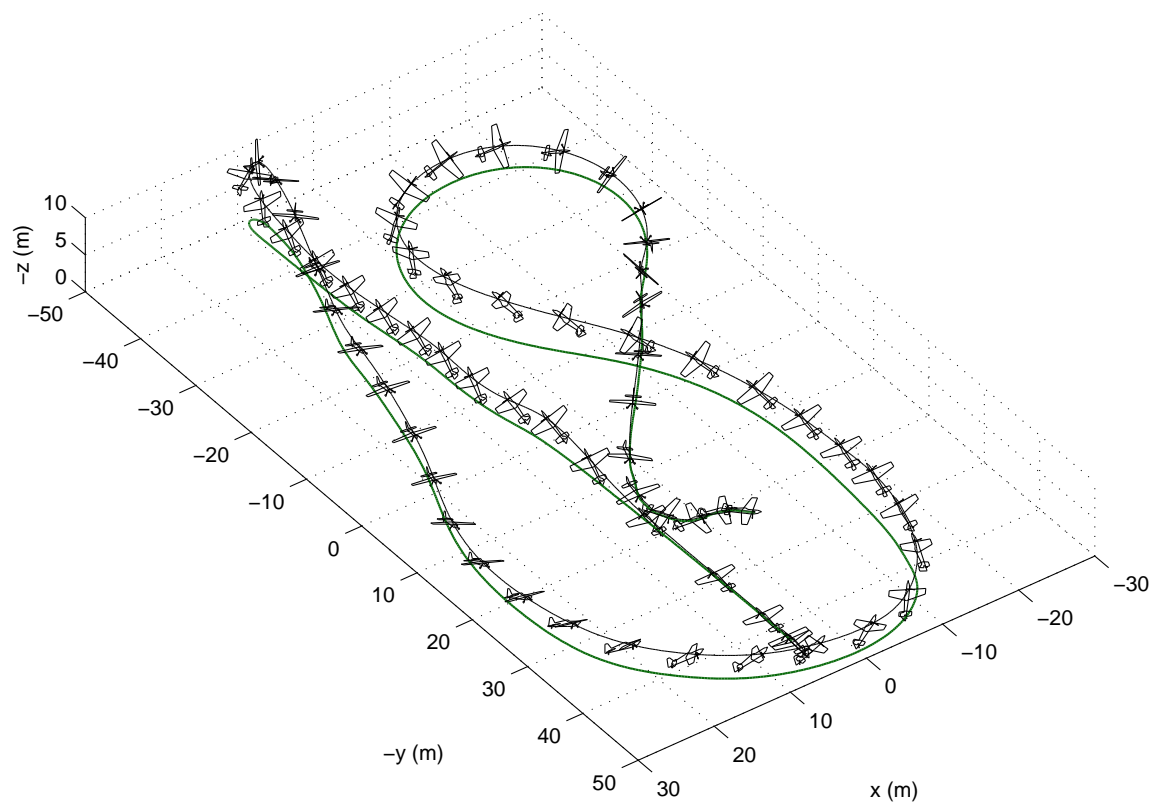
American Institute of Aeronautics and Astronautics

Figure 24. Time history of the 33%-scale Edge 540 aerobatic aircraft in a high angle of attack harrier (see Fig. 23 for trajectory).

American Institute of Aeronautics and Astronautics

Figure 25. Trajectory of the 33%-scale Edge 540 aerobatic aircraft in upright and inverted harriers [aircraft magnified 2 times normal size and drawn every 0.75 sec, wingspan of 2476.5 mm (97.5 in)].

American Institute of Aeronautics and Astronautics
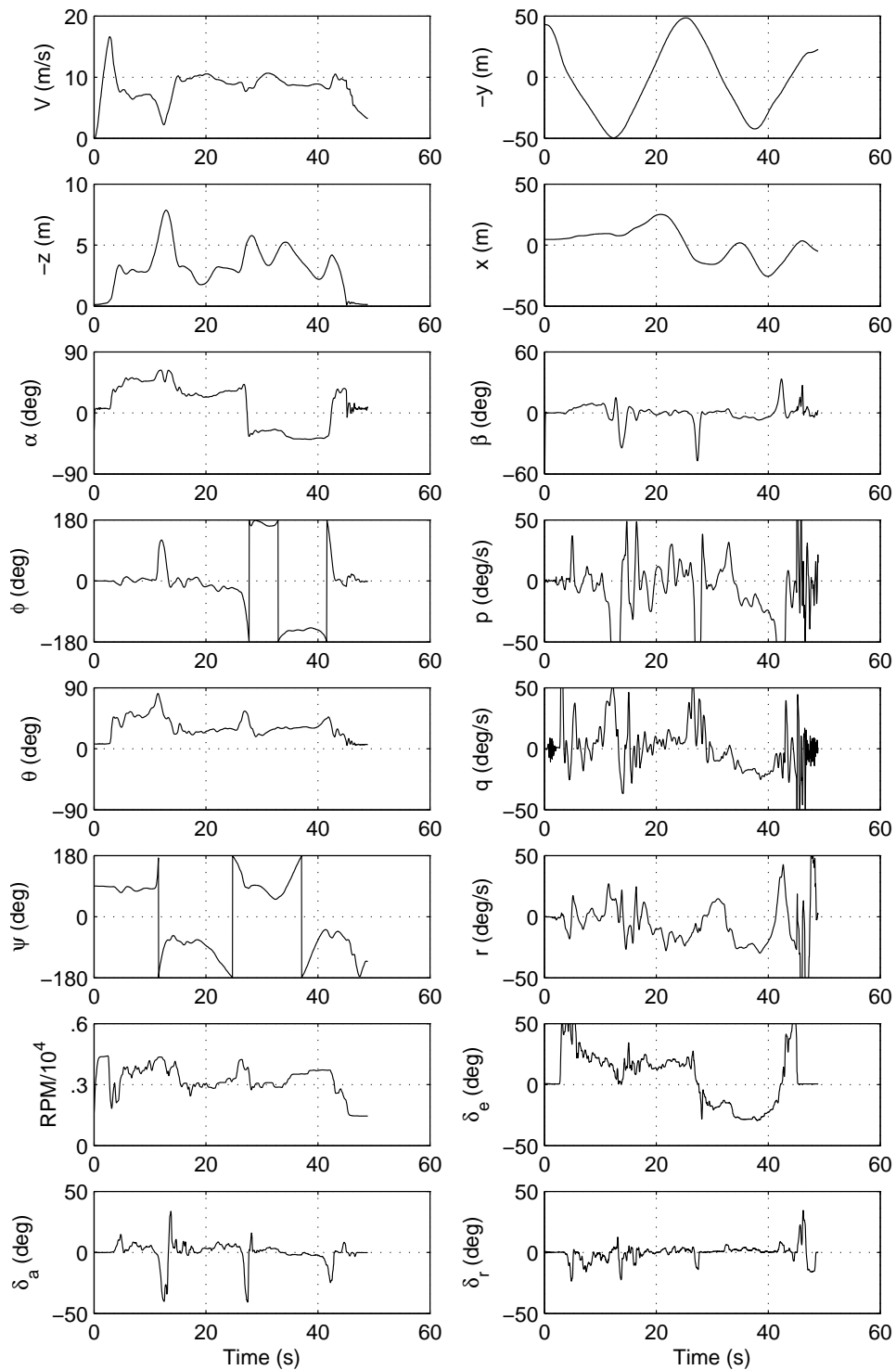
Figure 26. Time history of the 33%-scale Edge 540 aerobatic aircraft in upright and inverted harriers (see Fig. 25 for trajectory).

American Institute of Aeronautics and Astronautics

Figure 27. 46%-scale Ultimate TOC biplane used in simulations [rendering taken from simulator, wingspan of 2540 mm (100 in)].
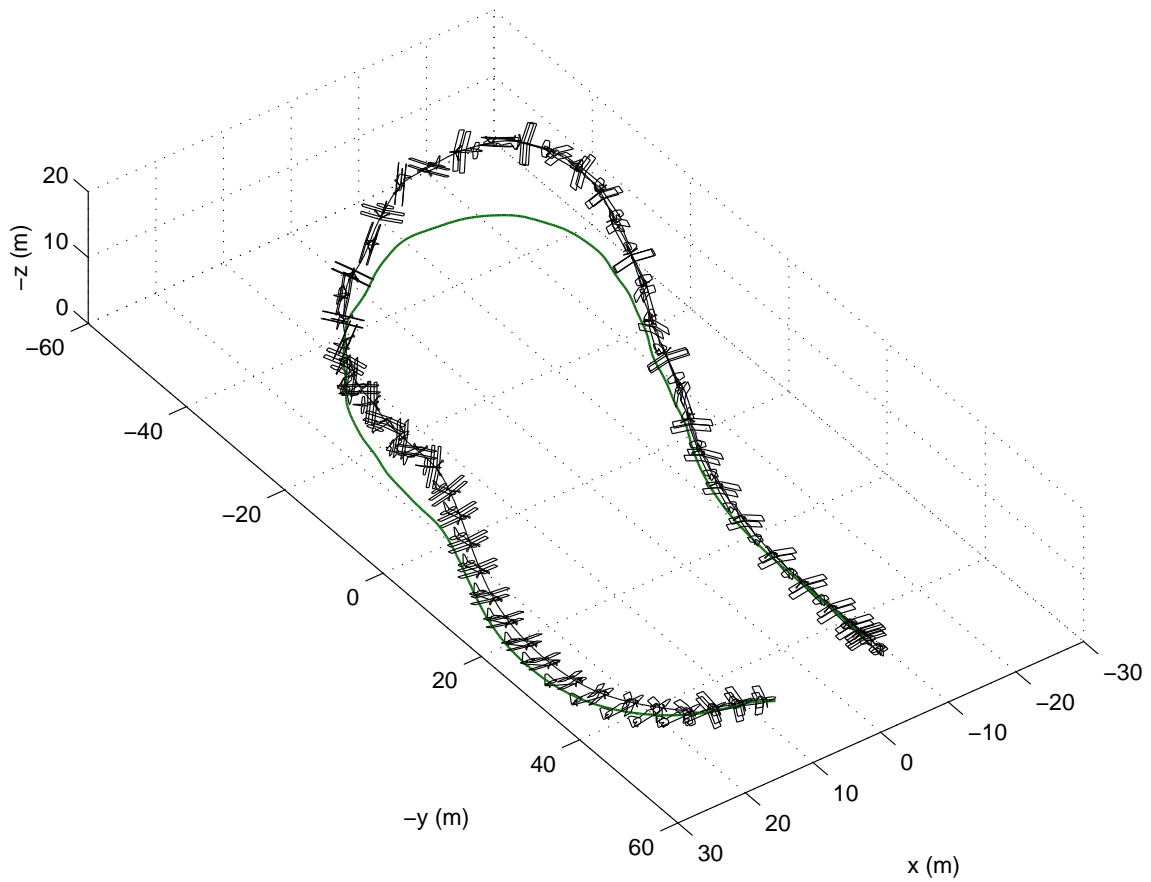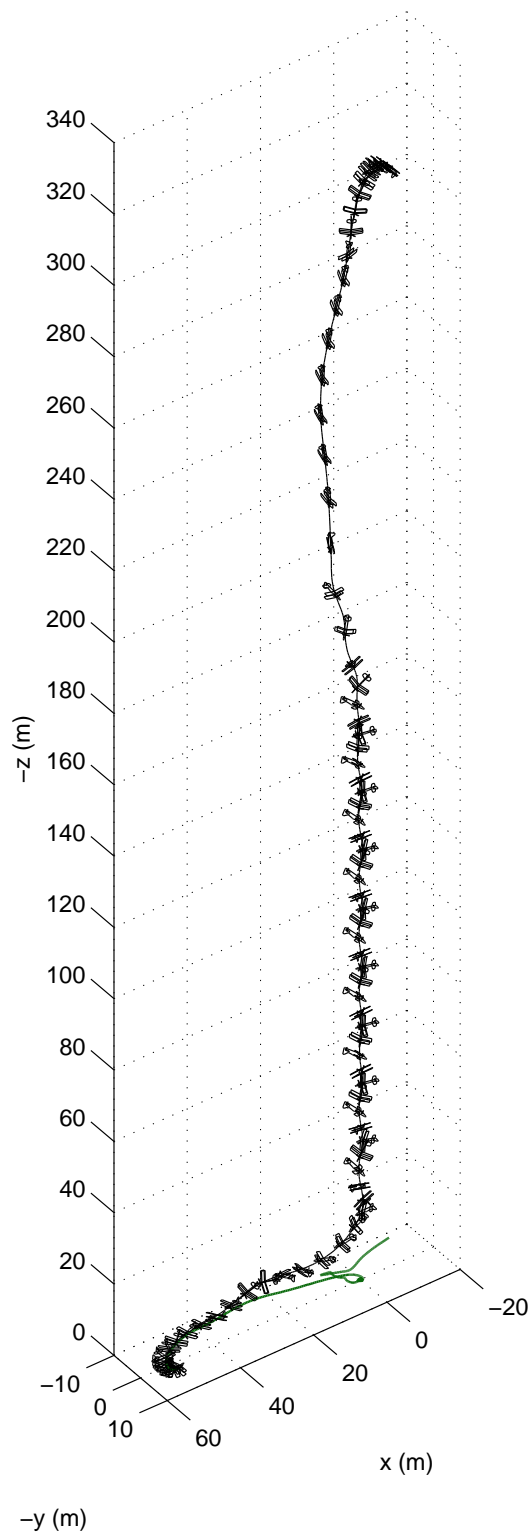

Figure 28. Trajectory of the 46%-scale Ultimate TOC aerobatic aircraft performing rolling harriers [aircraft magnified 2 times normal size and drawn every 0.45 sec, wingspan of 2540 mm (100 in)]

American Institute of Aeronautics and Astronautics
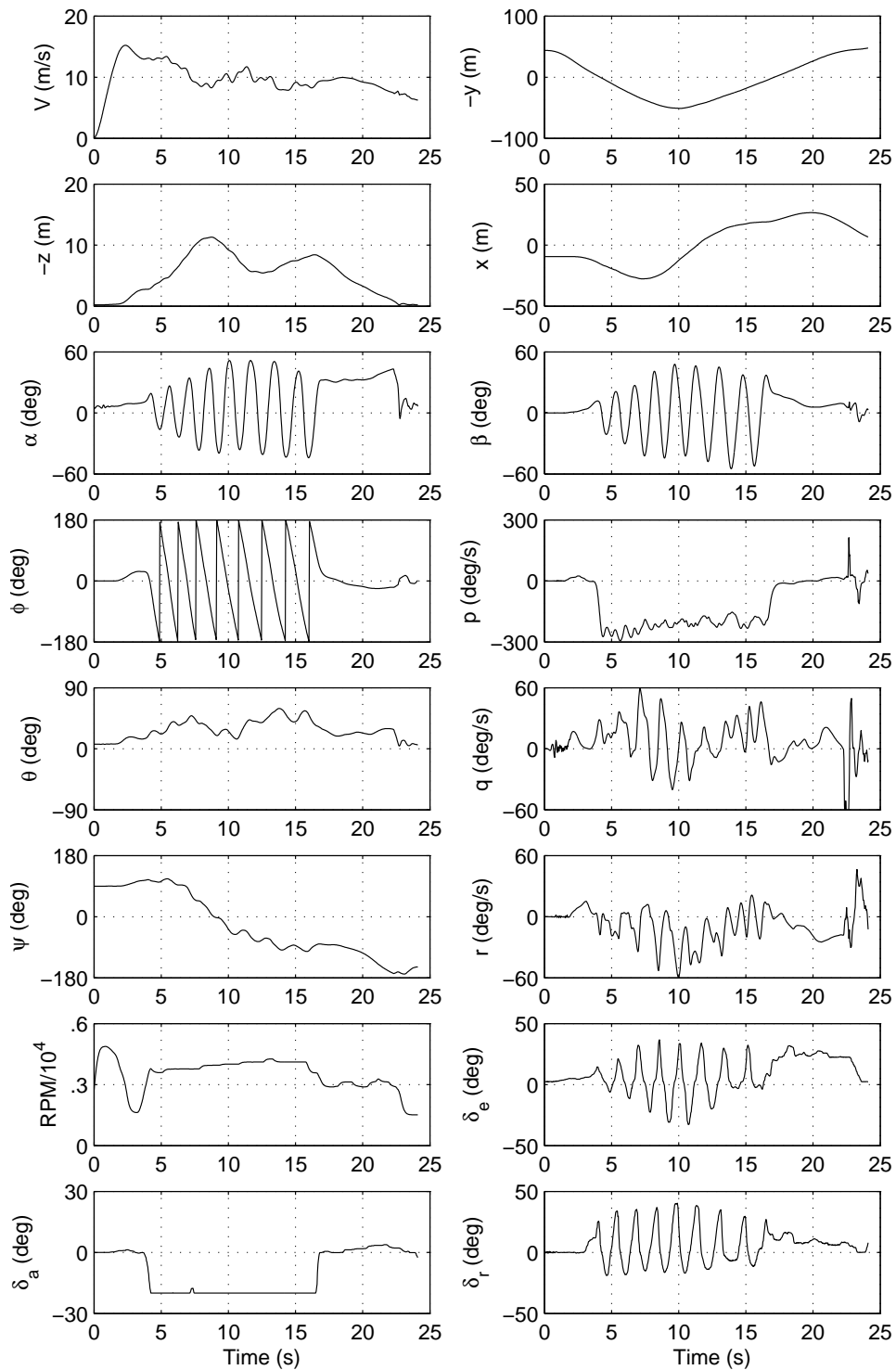
Figure 29. Time history of the 46%-scale Ultimate TOC aerobatic aircraft performing rolling harriers (see Fig. 28 for trajectory)

American Institute of Aeronautics and Astronautics

Figure 30. Trajectory of the 46%-scale Ultimate TOC aerobatic aircraft performing a blender / inverted spin [aircraft magnified 2 times normal size and drawn every 0.365 sec, wingspan of 2540 mm (100 in)]
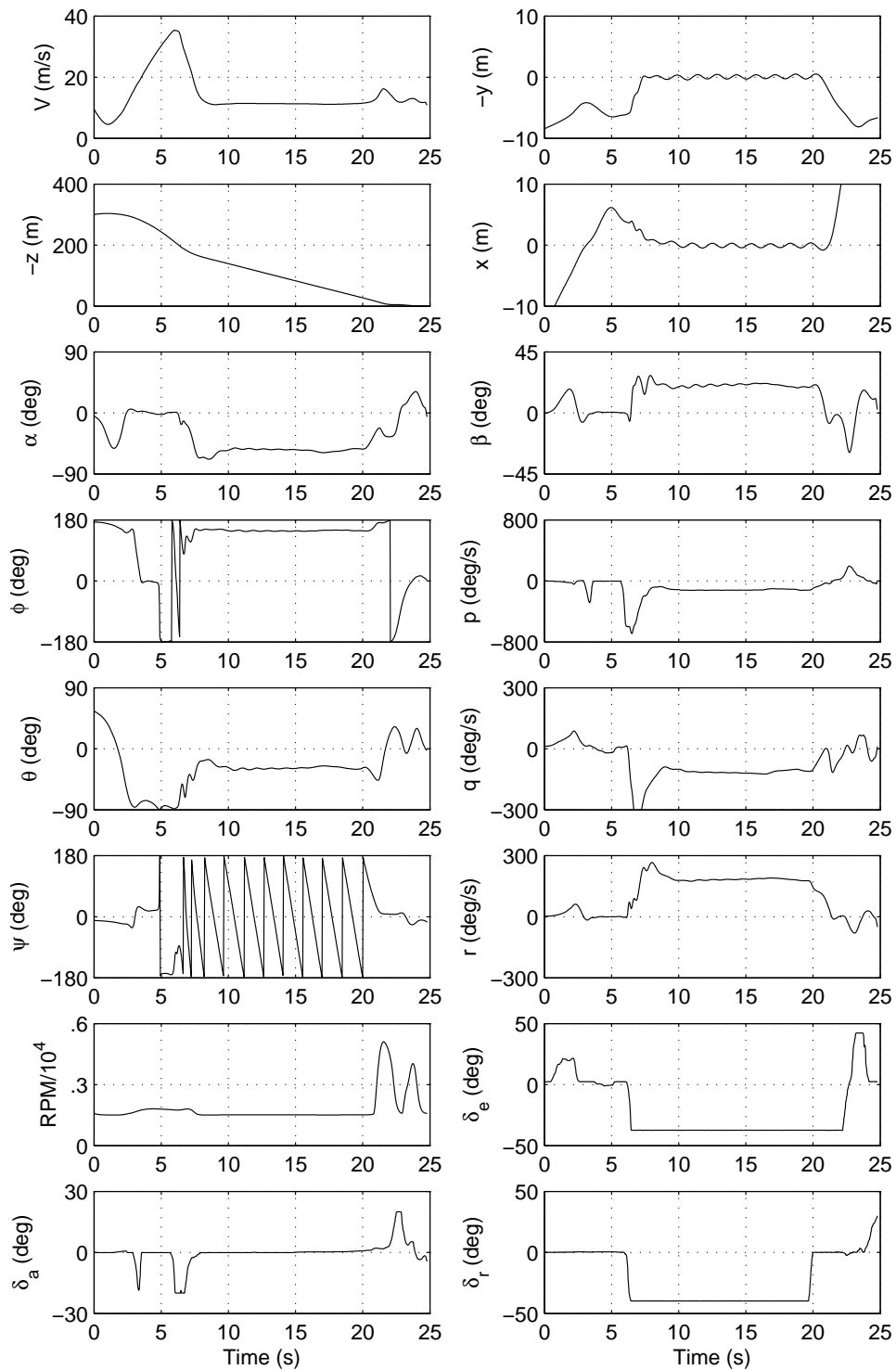
American Institute of Aeronautics and Astronautics

Figure 31. Time history of the 46%-scale Ultimate TOC aerobatic aircraft performing a blender / inverted spin (see Fig. 30 for trajectory)

American Institute of Aeronautics and Astronautics

Acknowledgments

References

[1]Taylor, D. J., OL, M. V., and Cord, T., "SkyTote: An Unmanned Precision Cargo Delivery System," AIAA Paper 2003–2753, July 2003.

[2]Blauwe, H. D., Bayraktar, S., Feron, E., and Lokumcu, F., "Flight Modeling and Experimental Autonomous Hover Control of a Fixed Wing Mini-UAV at High Angle of Attack," AIAA Paper 2007–6818, August 2007.

[3]Frank, A., McGrew, J. S., Valenti, M., Levine, D., and How, J. P., "Hover, Transition, and Level Flight Control Design for a Single-Propeller Indoor Airplane," AIAA Paper 2007–6318, August 2007.

[4]Sobolic, F. M. and How, J. P., "Nonlinear Agile Control Test Bed for a Fixed-Wing Aircraft in a Constrained Environment," AIAA Paper 2009–1927, April 2009.

[5]Kubo, D. and Suzuki, S., "Tail-Sitter Vertical Takeoff and Landing Unmanned Aerial Vehicle: Transitional Flight Analysis," *Journal of Aircraft*, Vol. 45, No. 1, 2008, pp. 292–297.

[6]Stone, R. H., "Aerodynamic Modeling of the Wing-Propeller Interaction for a Tail-Sitter Unmanned Air Vehicle," *Journal of Aircraft*, Vol. 45, No. 1, 2008, pp. 198–210.

[7]Stone, R. H., "Flight Testing of the T-Wing Tail-Sitter Unmanned Air Vehicle," *Journal of Aircraft*, Vol. 45, No. 2, 2008, pp. 673–685.

[8]Barlow, J. B., Rae, W. H., Jr., and Pope, A., *Low-Speed Wind Tunnel Testing, Third Ed.*, John Wiley and Sons, New York, 1999.

[9]Salas, M. D., "Digital Flight: The Last CFD Aeronautical Grand Challenge," *Journal of Scientific Computing*, Vol. 28, No. 213, September 2006, pp. 479–505.

[10]Mavriplis, D. J., Darmofal, D., Keyes, D., and Turner, M., "Petaflops Opportunities for the NASA Fundamental Aeronautics Program," AIAA Paper 2007–4084, June 2007.

[11]Tomac, M. and Rizzi, A., "Creation of Aerodynamic Database for the X-31," AIAA Paper 2010–501, January 2010.

[12]Ghoreyshi, M., Badcock, K. J., and Woodgate, M. A., "Accelerating the Numerical Generation of Aerodynamic Models for Flight Simulation," *Journal of Aircraft*, Vol. 46, No. 3, May–June 2010, pp. 972–980.

[13]Klein, V. and Morelli, E. A., *Aircraft System Identification: Theory and Practice*, AIAA Education Series, AIAA, Reston, VA, 2006.

[14]Jategaonkar, R. V., *Flight Vehicle System Identification: A Time Domain Methodology*, AIAA Progress in Astronautics and Aeronautics, AIAA, Reston, VA, 2006.

[15]Tobing, S., Go, T. H., and Vasilescu, R., "Improved Component Buildup Method for Fast Prediction of the Aerodynamic Performances of a Vertical Takeoff and Landing Micro Air Vehicle," *Computational Fluid Dynamics 2008*, Springer Berlin Heidelberg, 2009, pp. 209–214.

[16]Guerrero, I., Londenberg, K., Gelhausen, P., and Myklebust, A., "A Powered Lift Aerodynamic Analysis for the Design of Ducted Fan UAVs," AIAA Paper 2003–6567, September 2003.

[17]Evans, J. and Nahon, M., "Dynamics Modeling and Performance Evaluation of an Autonomous Underwater Vehicle," *Ocean Engineering*, Vol. 31, 2004, pp. 1835–1858.

[18]Saephan, S. and van Dam, C. P., "Determination of Wing-Only Aircraft Tumbling Characteristics through Computational Fluid Dynamics," *Journal of Aircraft*, Vol. 45, No. 3, May–June 2008, pp. 1044–1053.

[19]Phillips, W. F., *Mechanics of Flight*, John Wiley & Sons, New York, 2nd ed., 2010.

[20]Dickes, E. G. and Ralston, J. N., "Application of Large-Angle Data for Flight Simulation," AIAA Paper 2000–4584, August 2000.

[21]Foster, J. V., Cunningham, K., Fremaux, C. M., Shah, G. H., Stewart, E. C., Rivers, R. A., Wilborn, J. E., and Gato, W., "Dynamics Modeling and Simulation of Large Transport Airplanes in Upset Conditions," AIAA Paper 2005–5933, August 2005.

[22]Gingras, D. R. and Ralston, J. N., "Aerodynamics Modeling for Upset Training," AIAA Paper 2008–6870, August 2008.

[23]Keller, J. D., McKillip, R. M., Jr., and Wachspress, D. A., "Physical Modeling of Aircraft Upsets for Real-Time Simulation Applications," AIAA Paper 2008–6205, August 2008.

[24]Keller, J. D., McKillip, R. M., Jr., and Kim, S., "Aircraft Flight Envelope Determination using Upset Detection and Physical Modeling Methods," AIAA Paper 2009–6259, August 2009.

[25]"FS One, Precision RC Flight Simulator," Software Developed by InertiaSoft, Distributed by Horizon Hobby, Champaign, IL, 2006.

[26]Selig, M. S., "Modeling Propeller Aerodynamics and Slipstream Effects on Small UAVs in Realtime," AIAA Paper 2010–7938, August 2010.

[27]Uhlig, D. V., Selig, M. S., and Neogi, N., "Health Monitoring via Neural Networks," AIAA Paper 2010–3419, April 2010.

[28]Wright, J. R. and Cooper, J. E., *Introduction to Aircraft Aeroelasticity and Loads*, Aerospace Series, John Wiley & Sons, England, 2007.

[29]Johnson, W., *Helicopter Theory*, Dover, New York, 1980.

[30]McMillan, O. J., Schwind, R. G., Nielsen, J. N., and Dillenius, M. F. E., "Rolling Moments in a Trailing Vortex Flow Field," NEAR TR 129, also NASA CR-151961, February 1977.

[31]Poppen, A. P., Jr., "A Method for Estimating the Rolling Moment Due to Spin Rate for Arbitrary Planform Wings," NASA TM-86365, January 1985.

[32]Pamadi, B. N. and Taylor, L. W., Jr., "Estimation of Aerodynamic Forces and Moments on a Steadily Spinning Airplane," *Journal of Aircraft*, Vol. 21, No. 12, 1984, pp. 943–954.

[33]Pamadi, B. N., *Performance, Stability, Dynamics, and Control of Airplanes*, AIAA Education Series, AIAA, Reston, VA, 1998.

[34]Johnson, B. and Lind, R., "Characterizing Wing Rock with Variations in Size and Configuration of Vertical Tail," *Journal of Aircraft*, Vol. 47, No. 2, March–April 2010, pp. 567–576.

[35]Drela, M., "XFOIL: An Analysis and Design System for Low Reynolds Number Airfoils," *Low Reynolds Number Aerodynamics*, edited by T. J. Mueller, Vol. 54 of *Lecture Notes in Engineering*, Springer-Verlag, New York, June 1989, pp. 1–12.

[36]Ostowari, C. and Naik, D., "Post-Stall Wind Tunnel Data for NACA 44XX Series Airfoil Sections," SERI/STR-217-2559, January 1985.

[37]Sørensen, N. N., Johansen, J., and Conway, C., "CFD Computations of Wind Turbine Blade Loads During Standstill Operation KNOW-BLADE," Risø National Laboratory, Task 3.1 Report, Risø-R-1465(EN), June 2004.

[38]van Rooij, R. P. J. O. M., "Analysis of the Flow Characteristics of Two Nonrotating Rotor Blades," *Journal of Solar Energy Engineering*, Vol. 130, August 2008, 031015 (13 pages).

[39]Sørensen, N. N. and Michelsen, J. A., "Drag Prediction for Blades at High Angle of Attack Using CFD," *Journal of Solar Energy Engineering*, Vol. 126, No. 4, November 2004, pp. 1011–1016, [DOI:10.1115/1.1807854].

[40]Spera, D. A., "Models of Lift and Drag Coefficients of Stalled and Unstalled Airfoils in Wind Turbines and Wind Tunnels," NASA CR-2008-215434, October 2008.

[41]Lindenburg, C., "Stall Coefficients," Energy Research Center of the Netherlands, Petten, ECN-RX-01-004, January 2001, Presented at IEA Symposium on the Aerodynamics of Wind Turbines, National Renewable Energy Laboratory, Golden, CO, December, 2000.

[42]Tangler, J. L. and Ostowari, C., "Horizontal Axis Wind Turbine Post Stall Airfoil Characteristics Synthesization," Presented at the Horizontal-Axis Wind Turbine Technology Conference, Cleveland, OH, May, 1984.

[43]Montgomerie, B., "Methods for Root Effects, Tip Effects and Extending the Angle of Attack Range to ±180 deg, with Application to Aerodynamics for Blades on Wind Turbines and Propellers," Swedish Defence Research Agency, FOI-R-1305-SE, ISSN 1650-1942, June 2004.

[44]Ericsson, L. E., "Vortex Characteristics of Pitching Double-Delta Wings," *Journal of Aircraft*, Vol. 36, No. 2, March–April 1999, pp. 349–356.

[45]Leishman, J. G., *Principles of Helicopter Aerodynamics*, Cambridge Aerospace Series, Cambridge University Press, Cambridge, 2000.

[46]Zimmerman, C. H., "Characteristics of Clark Y Airfoils of Small Aspect Ratios," NACA TR-431, 1933.

[47]Zimmerman, C. H., "Aerodynamic Characteristics of Several Airfoils of Low Aspect Ratio," NACA TN-539, 1935.

[48]Silverstein, A. and Katzoff, S., "Aerodynamic Characteristics of Horizontal Tail Surfaces," NACA TR-688, 1940.

[49]Bates, W. R., "Collection and Analysis of Wind-Tunnel Data on the Characteristics of Isolated Tail Surfaces with and without End Plates ," NACA TN-1291, 1947.

[50]Whicker, L. F. and Fehlner, L. F., "Free-Stream Characteristics of a Family of Low-Aspect-Ratio, All-Movable Control Surfaces for Application to Ship Design," David Taylor Model Basin, Report 933, Washington, DC, December 1958.

[51]Koenig, D. G., "Low-Speed Tests of Semispan-Wing Models at Angles of Attack from 0° to 180°," NASA MEMO 2-27-59A, April 1959.

[52]Kerwin, J. W., Mandel, P., and Lewis, S. D., "An Experimental Study of a Series of Flapped Rudders," *Journal of Ship Research*, Vol. 16, No. 4, December 1972, pp. 221–239.

[53]Marchaj, C. A., *Sail Performance*, Adlard Coles Nautical, London, 1996.

[54]Marchaj, C. A., *Aero-Hydrodynamics of Sailing*, Dodd, Mead & Company, New York, 1979.

[55]Torres, G. and Mueller, T., "Low-Aspect-Ratio Wing Aerodynamics at Low Reynolds Numbers," *AIAA Journal*, Vol. 42, No. 5, May 2004, pp. 865–873.

[56]Desabrais, K. J., "Aerodynamic Forces on an Airdrop Platform," AIAA Paper 2005–1634, May 2005.

[57]Cosyn, P. and Vierendeels, J., "Numerical Investigation of Low-Aspect-Ratio Wings at Low Reynolds Numbers," *Journal of Aircraft*, Vol. 43, No. 3, May–June 2006, pp. 713–722.

[58]McCormick, B. W., *Aerodynamics, Aeronautics, and Flight Mechanics*, John Wiley & Sons, New York, 2nd ed., 1995.

[59]Hibbs, B. and Radkey, R. L., "Calculating Rotor Performance with the Revised PROP Computer Code," Tech. rep., Wind Energy Research Center, Rockwell International, Golden, CO, RFP-3508, UC-60, 1983.

[60]Selig, M. S. and Tangler, J. L., "Development and Application of a Multipoint Inverse Design Method for Horizontal Axis Wind Turbines," *Wind Engineering*, Vol. 19, No. 5, 1995, pp. 91–105.

[61]Selig, M. S., "PROPID - Software for Horizontal-Axis Wind Turbine Design and Analysis," http://www.ae.illinois.edu/m-selig/propid.html, 1995–.

[62]Sukumar, P. P. and Selig, M. S., "Dynamic Soaring of Sailplanes over Open Fields," AIAA Paper 2010–4953, June 2010.

American Institute of Aeronautics and Astronautics